

# Unique Spin Crossover Pathways Differentiated by Scan Rate in a New Dinuclear Fe(II) Triple Helicate: Mechanistic Deductions Enabled by Synchrotron Radiation Studies

*Matthew J. Wallis, Alexander R. Craze, Hikaru Zenno, Ryuya Tokunaga, Takahiro Taira,  
Hyunsung Min, Mohan M. Bhadbhade, Saroj Kumar Bhattacharyya, Ruoming Tian, Anne M.  
Rich, Shinya Hayami, Jack K. Clegg, Christopher E. Marjo, Leonard F. Lindoy and Feng Li\**

## **Corresponding Author**

**Feng Li** | PhD, FRSC, MRACI CChem - *School of Science, Western Sydney University,  
Locked Bag 1797, Penrith NSW 2751, Australia; Email: [feng.li@westernsydney.edu.au](mailto:feng.li@westernsydney.edu.au)*

## Supplementary Information

S1.	Crystallographic Refinement Details .....	3
S2.	Crystallographic data tables .....	4
S3.	Physical Measurements.....	1
S3.1.	Characterisation of ligand L .....	1
S3.2.	Characterisation of 1·6H <sub>2</sub> O .....	3
S4.	Mössbauer, SQUID and LIESST analysis of 1 .....	5
S4.1.	Mössbauer analysis of 1·6H <sub>2</sub> O and desolvated 1 .....	5
S4.2.	LIESST measurements of 1·6H <sub>2</sub> O and desolvated 1 .....	5
S5.	Variable temperature Raman spectroscopy.....	7
S6.	Intermolecular interactions of 1-MeCN .....	8
S7.	Scaling of crystal packing coefficient and molecular volume. ....	15
S8.	Helicate structural parameters.....	16
S8.1.	Linker torsion.....	17
S8.2.	Pitch and yaw .....	18
S8.3.	Chelate ring angles and bond axis .....	19
S9.	PXRD .....	21
S9.1.	PXRD Patterns .....	21
S9.2.	PXRD scan-rate dependent spectral differences.....	26
S9.3.	PXRD lattice parameters.....	28
S10.	References .....	30

## S1. Crystallographic Refinement Details

All but two crystal structures bore the triclinic space group  $P-1$ , with approximate cell length parameters  $a$ ,  $b$  and  $c$  of 16.2, 17.8 and 20.5 Å, respectively, and approximate angular parameters  $\alpha$ ,  $\beta$ ,  $\gamma$  of 80°, 90° and 75° respectively. In these structures, the resolved asymmetric unit contained a  $[\text{FeL}_3]^{4+}$  helicate, 4  $\text{BF}_4^-$  counterions, 4 acetonitriles, 1 diethyl ether and 0-6 water molecules, depending on the degree of disorder in the solvents. The exceptions of 1-MeCN@100/4 and 1-MeCN@150/4 crystal structures exhibited symmetry breaking, via the doubling of the  $c$ -axis and loss of half of the inversion centres together with a doubling of the molecules in the asymmetric unit. A solvent mask was applied in all crystal structures except 1-MeCN@100/relax to account for the electron density of all poorly resolved water molecules. In well-ordered structures, the entire helicate molecule was refined anisotropically. Several structures exhibited disorder in chelate rings, linkers and terminal moieties. In disordered structures the restraints DFIX, DANG, SADI, FLAT and RIGU were used to appropriately model various groups. Terminal and linker groups were split in structures where they could be resolved at distinct positions and refined against free variables. Where satisfactory anisotropic modelling was not possible, sections of the helicate were modelled isotropically.  $\text{BF}_4^-$  counterions and solvents were modelled anisotropically where possible; the restraints DFIX, DANG, SADI and RIGU were implemented where appropriate and in some cases idealised rigid bodies were used for modelling.<sup>1</sup> Where multiple positions could be resolved, molecules were split and refined against free variables. Hydrogen atoms were fixed using a riding model, though some were removed to allow convergence of shifts to zero.

## S2. Crystallographic data tables

Table S1. Crystallographic data for 1-MeCN at 250 K, after full relaxation at 100 K, after flash cooling to 100 K and at a scan rate of 4 K min<sup>-1</sup>.

Temperature (K) / Scan rate (K min <sup>-1</sup> )	250 (mounted at 250 K)	100/Relax	100/Flash	100/4	150/4	200/4
CCDC Number	2215606	2215607	2215608	2215605	2215604	2215603
Empirical formula	C <sub>102</sub> H <sub>88</sub> B <sub>4</sub> F <sub>16</sub> Fe <sub>2</sub> N <sub>28</sub> O <sub>4</sub>	C <sub>102</sub> H <sub>88</sub> B <sub>4</sub> F <sub>16</sub> Fe <sub>2</sub> N <sub>28</sub> O <sub>9.75</sub>	C <sub>102</sub> H <sub>72</sub> B <sub>4</sub> F <sub>16</sub> Fe <sub>2</sub> N <sub>28</sub> O <sub>4.25</sub>	C <sub>102</sub> H <sub>66</sub> B <sub>4</sub> F <sub>16</sub> Fe <sub>2</sub> N <sub>28</sub> O <sub>4.38</sub>	C <sub>100</sub> H <sub>71.5</sub> B <sub>4</sub> F <sub>16</sub> Fe <sub>2</sub> N <sub>2</sub> <sub>8</sub> O <sub>3.62</sub>	C <sub>102</sub> H <sub>85</sub> B <sub>4</sub> F <sub>16</sub> Fe <sub>2</sub> N <sub>28</sub> O <sub>4.25</sub>
Formula weight	2228.94	2320.94	2216.81	2212.76	2182.29	2229.91
Temperature (K)	250.00	100.00	100	100.00	150.00	200.00
Crystal system	triclinic	triclinic	triclinic	triclinic	triclinic	triclinic
Space group	P-1	P-1	P-1	P-1	P-1	P-1
<i>a</i> (Å)	16.220(3)	16.2552(12)	16.170(3)	16.200(3)	16.213(3)	16.170(3)
<i>b</i> (Å)	18.180(4)	16.7337(13)	17.720(4)	17.690(4)	17.771(4)	17.980(4)
<i>c</i> (Å)	20.750(4)	20.6466(16)	20.400(4)	40.670(8)	40.795(8)	20.660(4)
$\alpha$ (°)	79.51(3)	95.700(2)	80.66(3)	80.68(3)	80.50(3)	79.96(3)
$\beta$ (°)	88.31(3)	90.632(2)	89.87(3)	89.96(3)	89.67(3)	89.02(3)
$\gamma$ (°)	72.75(3)	106.361(2)	72.53(3)	72.52(3)	72.56(3)	72.68(3)
Volume (Å <sup>3</sup> )	5744(2)	5357.5(7)	5495(2)	10956(4)	11048(4)	5643(2)
<i>Z</i>	2	2	2	4	4	2
$\rho_{\text{calc}}$ (g cm <sup>-3</sup> )	1.289	1.439	1.340	1.342	1.312	1.312
$\mu$ (mm <sup>-1</sup> )	0.339	0.370	0.354	0.355	0.351	0.345
F(000)	2288.0	2380.0	2260.0	4500.0	4450.0	2286.0
Crystal size (mm <sup>3</sup> )	0.2 × 0.1 × 0.02	0.2 × 0.1 × 0.02	0.2 × 0.1 × 0.02	0.2 × 0.1 × 0.02	0.2 × 0.1 × 0.02	0.2 × 0.1 × 0.01
Radiation	MoK $\alpha$ ( $\lambda$ = 0.71073)	MoK $\alpha$ ( $\lambda$ = 0.71073)	MoK $\alpha$ ( $\lambda$ = 0.71073)	MoK $\alpha$ ( $\lambda$ = 0.71073)	MoK $\alpha$ ( $\lambda$ = 0.71073)	MoK $\alpha$ ( $\lambda$ = 0.71073)
2 $\theta$ range for data collection (°)	1.996 to 57.286	3.968 to 41.748	2.026 to 57.222	1.016 to 57.476	1.014 to 57.364	2.004 to 57.084
Index ranges	-20 ≤ <i>h</i> ≤ 21, -23 ≤ <i>k</i> ≤ 24, -25 ≤ <i>l</i> ≤ 25	-16 ≤ <i>h</i> ≤ 16, -16 ≤ <i>k</i> ≤ 16, -20 ≤ <i>l</i> ≤ 20	-21 ≤ <i>h</i> ≤ 21, -23 ≤ <i>k</i> ≤ 23, -26 ≤ <i>l</i> ≤ 27	-21 ≤ <i>h</i> ≤ 21, -23 ≤ <i>k</i> ≤ 23, -52 ≤ <i>l</i> ≤ 52	? ≤ <i>h</i> ≤ ?, ? ≤ <i>k</i> ≤ ?, ? ≤ <i>l</i> ≤ ?	-21 ≤ <i>h</i> ≤ 21, -24 ≤ <i>k</i> ≤ 23, -26 ≤ <i>l</i> ≤ 26

Temperature (K) / Scan rate (K min <sup>-1</sup> )	250 (mounted at 250 K)	100/Relax	100/Flash	100/4	150/4	200/4
Reflections collected	142373	131246	135886	265003	44873	138000
Independent reflections	23835 [R <sub>int</sub> = 0.0345, R <sub>sigma</sub> = 0.0225]	11276 [R <sub>int</sub> = 0.0656, R <sub>sigma</sub> = 0.0274]	22448 [R <sub>int</sub> = 0.0235, R <sub>sigma</sub> = 0.0150]	44565 [R <sub>int</sub> = 0.0418, R <sub>sigma</sub> = 0.0291]	44873 [R <sub>int</sub> = 0.0455, R <sub>sigma</sub> = 0.0223]	23020 [R <sub>int</sub> = 0.0209, R <sub>sigma</sub> = 0.0142]
Data/restraints/parameters	23835/588/1404	11276/6/1440	22448/1580/1907	44565/1746/3144	44873/1950/3116	23020/1216/1789
Goodness-of-fit on F <sup>2</sup>	1.083	1.070	1.878	1.811	1.769	1.035
Final R indexes [I ≥ 2σ(I)]	R <sub>1</sub> = 0.0791, wR <sub>2</sub> = 0.2486	R <sub>1</sub> = 0.0756, wR <sub>2</sub> = 0.1856	R <sub>1</sub> = 0.1183, wR <sub>2</sub> = 0.4020	R <sub>1</sub> = 0.1484, wR <sub>2</sub> = 0.4366	R <sub>1</sub> = 0.1428, wR <sub>2</sub> = 0.4226	R <sub>1</sub> = 0.0832, wR <sub>2</sub> = 0.2585
Final R indexes [all data]	R <sub>1</sub> = 0.0965, wR <sub>2</sub> = 0.2716	R <sub>1</sub> = 0.0871, wR <sub>2</sub> = 0.1953	R <sub>1</sub> = 0.1332, wR <sub>2</sub> = 0.4240	R <sub>1</sub> = 0.1846, wR <sub>2</sub> = 0.4696	R <sub>1</sub> = 0.1743, wR <sub>2</sub> = 0.4518	R <sub>1</sub> = 0.0947, wR <sub>2</sub> = 0.2730
Largest diff. peak/hole / e Å <sup>-3</sup>	0.83/-1.19	1.47/-0.83	1.22/-1.09	2.29/-1.11	2.15/-0.88	1.32/-0.66

Table S2. Crystallographic data for **1** at scan rates 1 K min<sup>-1</sup> and 2 K min<sup>-1</sup>.

Temperature (K) / Scan rate (K min <sup>-1</sup> )	100/1	150/1	200/1	100/2	150/2	200/2
CCDC Number	2215599	2215598	2215597	2215602	2215601	2215600
Empirical formula	C <sub>101</sub> H <sub>79</sub> B <sub>4</sub> F <sub>16</sub> Fe <sub>2</sub> N <sub>27.5</sub> O <sub>4.25</sub>	C <sub>102</sub> H <sub>82</sub> B <sub>4</sub> F <sub>16</sub> Fe <sub>2</sub> N <sub>28</sub> O <sub>4.25</sub>	C <sub>102</sub> H <sub>82</sub> B <sub>4</sub> F <sub>16</sub> Fe <sub>2</sub> N <sub>28</sub> O <sub>4.25</sub>	C <sub>102</sub> H <sub>79</sub> B <sub>4</sub> F <sub>16</sub> Fe <sub>2</sub> N <sub>28</sub> O <sub>4</sub>	C <sub>102</sub> H <sub>82</sub> B <sub>4</sub> F <sub>16</sub> Fe <sub>2</sub> N <sub>28</sub> O <sub>4</sub>	C <sub>102</sub> H <sub>82</sub> B <sub>4</sub> F <sub>16</sub> Fe <sub>2</sub> N <sub>28</sub> O <sub>4.25</sub>
Formula weight	2204.85	2226.89	2226.89	2219.87	2222.89	2226.89
Temperature (K)	100.00	150.00	200.00	100.00	150.00	200.00
Crystal system	triclinic	triclinic	triclinic	triclinic	triclinic	triclinic
Space group	P-1	P-1	P-1	P-1	P-1	P-1
<i>a</i> (Å)	16.220(3)	16.230(3)	16.190(3)	16.190(3)	16.220(3)	16.230(3)
<i>b</i> (Å)	17.820(4)	17.910(4)	18.080(4)	17.720(4)	17.830(4)	18.070(4)
<i>c</i> (Å)	20.390(4)	20.470(4)	20.660(4)	20.520(4)	20.570(4)	20.630(4)
<i>α</i> (°)	80.28(3)	80.13(3)	79.71(3)	80.09(3)	79.97(3)	79.64(3)

Temperature (K) / Scan rate (K min <sup>-1</sup> )	100/1	150/1	200/1	100/2	150/2	200/2
$\beta$ (°)	89.54(3)	89.33(3)	88.79(3)	89.48(3)	89.25(3)	88.86(3)
$\gamma$ (°)	72.46(3)	72.51(3)	72.69(3)	72.58(3)	72.52(3)	72.60(3)
Volume (Å <sup>3</sup> )	5533(2)	5586(2)	5678(2)	5527(2)	5583(2)	5676(2)
Z	2	2	2	2	2	2
$\rho_{\text{calc}}$ (g cm <sup>-3</sup> )	1.323	1.324	1.303	1.334	1.322	1.303
$\mu$ (mm <sup>-1</sup> )	0.351	0.349	0.343	0.352	0.349	0.343
F(000)	2255.0	2280.0	2280.0	2270.0	2276.0	2280.0
Crystal size (mm <sup>3</sup> )	0.2 × 0.1 × 0.02	0.2 × 0.1 × 0.02	0.2 × 0.1 × 0.02	0.2 × 0.1 × 0.02	0.2 × 0.1 × 0.02	0.2 × 0.1 × 0.02
Radiation	MoK $\alpha$ ( $\lambda$ = 0.71073)	MoK $\alpha$ ( $\lambda$ = 0.71073)	MoK $\alpha$ ( $\lambda$ = 0.71073)	MoK $\alpha$ ( $\lambda$ = 0.71073)	MoK $\alpha$ ( $\lambda$ = 0.71073)	MoK $\alpha$ ( $\lambda$ = 0.71073)
2 $\Theta$ range for data collection (°)	2.028 to 57.352	2.022 to 57.396	2.004 to 57.384	2.016 to 57.372	2.012 to 57.302	2.008 to 57.384
Index ranges	-20 ≤ h ≤ 20, -23 ≤ k ≤ 23, -25 ≤ l ≤ 25	-20 ≤ h ≤ 20, -23 ≤ k ≤ 23, -26 ≤ l ≤ 25	-20 ≤ h ≤ 20, -23 ≤ k ≤ 23, -26 ≤ l ≤ 26	-21 ≤ h ≤ 21, -23 ≤ k ≤ 23, -27 ≤ l ≤ 27	-21 ≤ h ≤ 21, -24 ≤ k ≤ 23, -27 ≤ l ≤ 27	-21 ≤ h ≤ 21, -24 ≤ k ≤ 24, -26 ≤ l ≤ 27
Reflections collected	137720	139097	140644	135105	136769	138164
Independent reflections	22920 [R <sub>int</sub> = 0.0210, R <sub>sigma</sub> = 0.0143]	23111 [R <sub>int</sub> = 0.0238, R <sub>sigma</sub> = 0.0162]	23499 [R <sub>int</sub> = 0.0236, R <sub>sigma</sub> = 0.0153]	22889 [R <sub>int</sub> = 0.0250, R <sub>sigma</sub> = 0.0138]	23161 [R <sub>int</sub> = 0.0201, R <sub>sigma</sub> = 0.0126]	23548 [R <sub>int</sub> = 0.0287, R <sub>sigma</sub> = 0.0178]
Data/restraints/param eters	22920/1589/1525	23111/1543/1596	23499/743/1584	22889/1130/1397	23161/1175/1378	23548/1179/1675
Goodness-of-fit on F <sup>2</sup>	2.583	2.163	1.077	2.340	2.321	1.511
Final R indexes [I ≥ 2 $\sigma$ (I)]	R <sub>1</sub> = 0.1792, wR <sub>2</sub> = 0.5405	R <sub>1</sub> = 0.1510, wR <sub>2</sub> = 0.4755	R <sub>1</sub> = 0.0690, wR <sub>2</sub> = 0.2166	R <sub>1</sub> = 0.1379, wR <sub>2</sub> = 0.4567	R <sub>1</sub> = 0.1316, wR <sub>2</sub> = 0.4519	R <sub>1</sub> = 0.0858, wR <sub>2</sub> = 0.3045
Final R indexes [all data]	R <sub>1</sub> = 0.2039, wR <sub>2</sub> = 0.5741	R <sub>1</sub> = 0.1755, wR <sub>2</sub> = 0.5091	R <sub>1</sub> = 0.0803, wR <sub>2</sub> = 0.2324	R <sub>1</sub> = 0.1447, wR <sub>2</sub> = 0.4733	R <sub>1</sub> = 0.1384, wR <sub>2</sub> = 0.4696	R <sub>1</sub> = 0.0904, wR <sub>2</sub> = 0.3181
Largest diff. peak/hole / e Å <sup>-3</sup>	1.59/-1.05	1.66/-1.02	0.98/-0.74	1.80/-0.87	1.76/-0.88	1.28/-0.77

**Table S3.** Table of coordinate bond length in all SCXRD structures. Note that labels G, H and I were used to label the ligands A, B and C, respectively for the [MS-MS] helicate species found in **1@100/4** and **1@150/4**.

Coordinate Bond	<b>1@250</b>	<b>1@100/Relax</b>	<b>1@100/Flash</b>	<b>1@100/1</b>	<b>1@150/1</b>	<b>1@200/1</b>	<b>1@100/2</b>	<b>1@150/2</b>	<b>1@200/2</b>	<b>1@100/4</b>	<b>1@150/4</b>	<b>1@200/4</b>
CCDC Number	2215606	2215607	2215608	2215599	2215598	2215597	2215602	2215601	2215600	2215605	2215604	2215603
Fe1—N3A (Å)	2.168 (3)	2.166 (5)	2.125 (5)	2.135 (8)	2.151 (7)	2.169 (2)	2.121 (4)	2.138 (4)	2.159 (2)	2.170 (7)	2.138 (5)	2.168 (3)
Fe1—N3B (Å)	2.137 (3)	2.136 (5)	2.105 (5)	2.079 (8)	2.096 (6)	2.129 (2)	2.091 (4)	2.092 (4)	2.126 (2)	2.206 (8)	2.108 (5)	2.124 (3)
Fe1—N3C (Å)	2.169 (3)	2.166 (5)	2.119 (5)	2.094 (7)	2.121 (6)	2.168 (2)	2.108 (4)	2.118 (4)	2.162 (2)	2.144 (6)	2.149 (5)	2.169 (3)
Fe1—N4A (Å)	2.249 (3)	2.212 (5)	2.196 (7)	2.123 (10)	2.206 (8)	2.243 (3)	2.158 (5)	2.173 (5)	2.239 (3)	2.137 (6)	2.222 (6)	2.243 (3)
Fe1—N4B (Å)	2.236 (3)	2.262 (5)	2.209 (5)	2.197 (7)	2.200 (6)	2.230 (2)	2.175 (4)	2.193 (4)	2.228 (2)	2.125 (6)	2.242 (5)	2.231 (3)
Fe1—N4C (Å)	2.212 (3)	2.211 (5)	2.176 (5)	2.168 (7)	2.184 (6)	2.211 (2)	2.160 (5)	2.178 (4)	2.200 (2)	2.144 (6)	2.205 (5)	2.210 (3)
Fe2—N5A (Å)	2.246 (3)	2.017 (5)	2.109 (6)	2.126 (9)	2.147 (7)	2.241 (3)	2.109 (5)	2.149 (5)	2.226 (3)	1.980 (6)	2.018 (5)	2.225 (3)
Fe2—N5B (Å)	2.228 (3)	2.012 (5)	2.090 (4)	2.100 (5)	2.130 (5)	2.220 (2)	2.114 (4)	2.127 (4)	2.204 (2)	2.017 (5)	2.027 (4)	2.207 (3)
Fe2—N5C (Å)	2.231 (3)	2.009 (5)	2.100 (4)	2.115 (5)	2.151 (4)	2.224 (3)	2.109 (4)	2.126 (4)	2.216 (2)	2.053 (4)	2.066 (4)	2.211 (3)
Fe2—N6A (Å)	2.138 (3)	1.982 (5)	2.042 (4)	2.065 (6)	2.093 (5)	2.134 (2)	2.040 (4)	2.059 (4)	2.128 (2)	1.983 (5)	1.999 (5)	2.126 (3)
Fe2—N6B (Å)	2.156 (3)	1.977 (5)	2.052 (3)	2.059 (5)	2.081 (4)	2.149 (2)	2.057 (4)	2.071 (3)	2.139 (2)	2.007 (4)	2.007 (4)	2.135 (3)
Fe2—N6C (Å)	2.167 (3)	1.979 (5)	2.054 (3)	2.041 (5)	2.068 (5)	2.159 (3)	2.054 (4)	2.073 (3)	2.155 (2)	1.983 (5)	1.987 (4)	2.147 (3)
Fe1'—N3G (Å)	—	—	—	—	—	—	—	—	—	2.100 (6)	2.116 (6)	—
Fe1'—N3H (Å)	—	—	—	—	—	—	—	—	—	2.113 (6)	2.124 (5)	—
Fe1'—N3I (Å)	—	—	—	—	—	—	—	—	—	2.157 (7)	2.158 (7)	—
Fe1'—N4G (Å)	—	—	—	—	—	—	—	—	—	2.170 (7)	2.208 (6)	—
Fe1'—N4H (Å)	—	—	—	—	—	—	—	—	—	2.206 (8)	2.211 (7)	—
Fe1'—N4I (Å)	—	—	—	—	—	—	—	—	—	2.144 (6)	2.172 (6)	—
Fe2'—N5G (Å)	—	—	—	—	—	—	—	—	—	2.200 (8)	2.238 (7)	—
Fe2'—N5H (Å)	—	—	—	—	—	—	—	—	—	2.164 (5)	2.187 (5)	—
Fe2'—N5I (Å)	—	—	—	—	—	—	—	—	—	2.177 (5)	2.193 (4)	—
Fe2'—N6G (Å)	—	—	—	—	—	—	—	—	—	2.097 (5)	2.116 (5)	—
Fe2'—N6H (Å)	—	—	—	—	—	—	—	—	—	2.117 (5)	2.122 (5)	—
Fe2'—N6I (Å)	—	—	—	—	—	—	—	—	—	2.116 (5)	2.134 (5)	—

### S3. Physical Measurements

#### S3.1. Characterisation of ligand L

The  $^1\text{H}$  NMR and  $^{13}\text{C}$  NMR (Figures S1,S2) confirmed the formation of ligand L. The high-resolution ESI-MS (HR ESI-MS) of L identified  $m/z$  values at 511.2010 and 533.1523, which correspond to  $[\text{L}+\text{H}]^+$  and  $[\text{L}+\text{Na}]^+$  respectively (Figure S3). The isotopic pattern for both charged species of L is in good accordance with their simulated isotopic distributions.

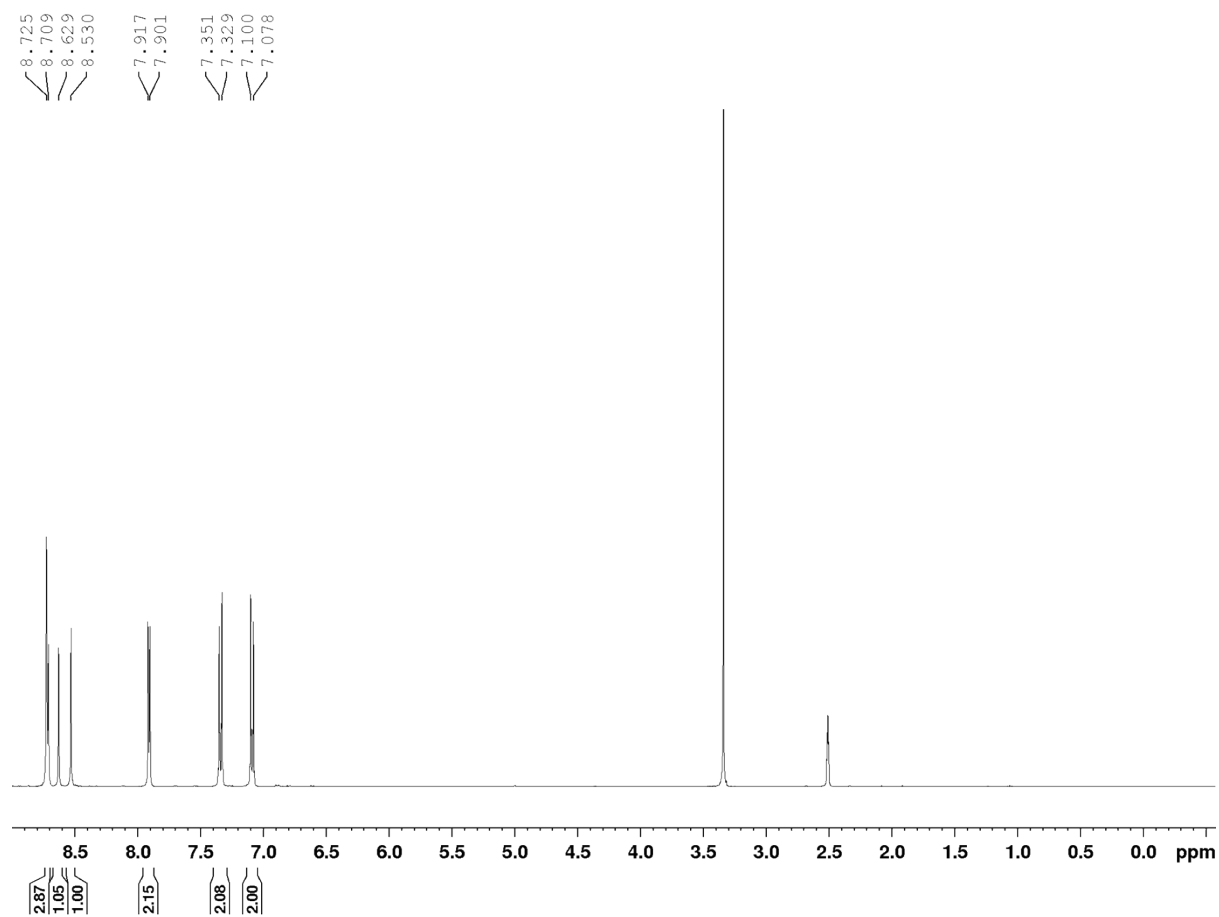


**Figure S1.**  $^1\text{H}$  NMR spectrum of L (DMSO- $d_6$ , 400MHz)



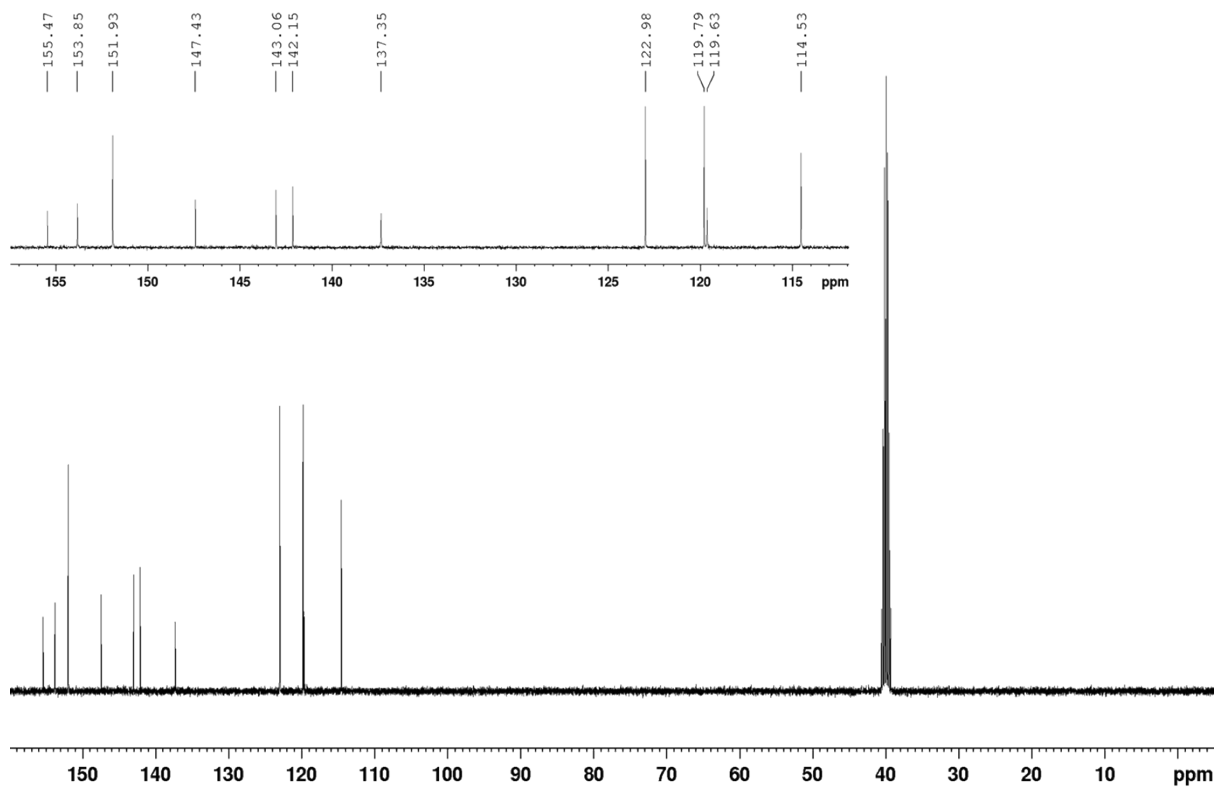


**Figure S2.**  $^{13}\text{C}$  NMR spectrum of **L** ( $\text{DMSO-d}_6$ , 100MHz).

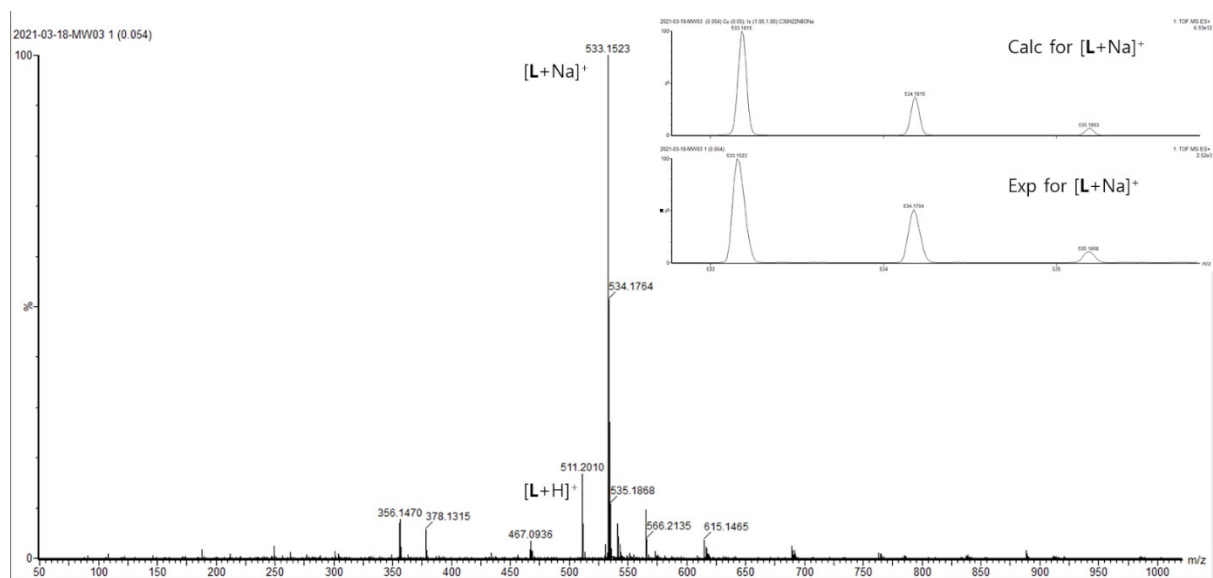


**Figure S3.** HR ESI(+)-MS spectrum of **L** in methanol. The inset identifies the isotopic pattern of  $[\text{L}+\text{Na}]^+$  (bottom) with simulated pattern (top).

### S3.2. Characterisation of 1·6H<sub>2</sub>O

The HR ESI-MS of **1** gave  $m/z$  values at 410.5572, 576.4459 and 908.1909 which corresponds to  $[\text{Fe}_2\text{L}_3]^{4+}$ ,  $[\text{Fe}_2\text{L}_3(\text{BF}_4)]^{3+}$  and  $[\text{Fe}_2\text{L}_3(\text{BF}_4)_2]^{2+}$  respectively (Figure S4). The isotopic patterns of all charged species of the metalloligand are in good agreement with their simulated isotopic distributions. SEM-EDS analysis of **1**, the EDS spectrum confirmed the presence of C, N, F, O and Fe (Figure S5). Simultaneous thermal analysis (STA) was consistent with the finding from the CHN experimental finding of 6 H<sub>2</sub>O molecules in solvated **1** (Figure S6).

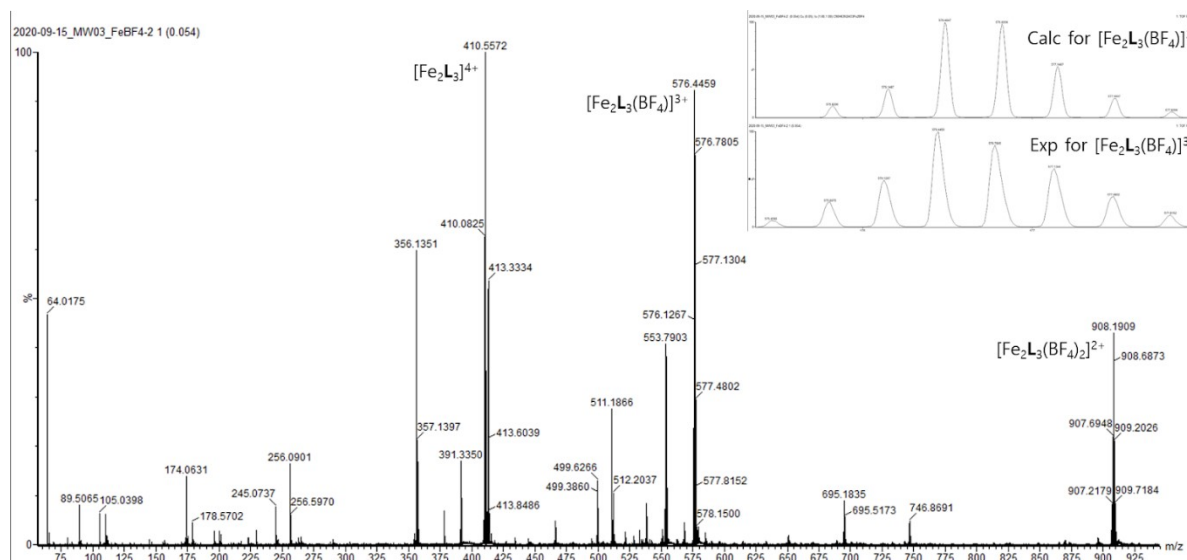


**Figure S4.** HR ESI(+)-MS spectrum of  $[\text{Fe}_2\text{L}_3(\text{BF}_4)_4]$  in acetonitrile. The inset shows the isotopic pattern of  $[\text{Fe}_2\text{L}_3(\text{BF}_4)]^{3+}$  (bottom) with simulated pattern (top).

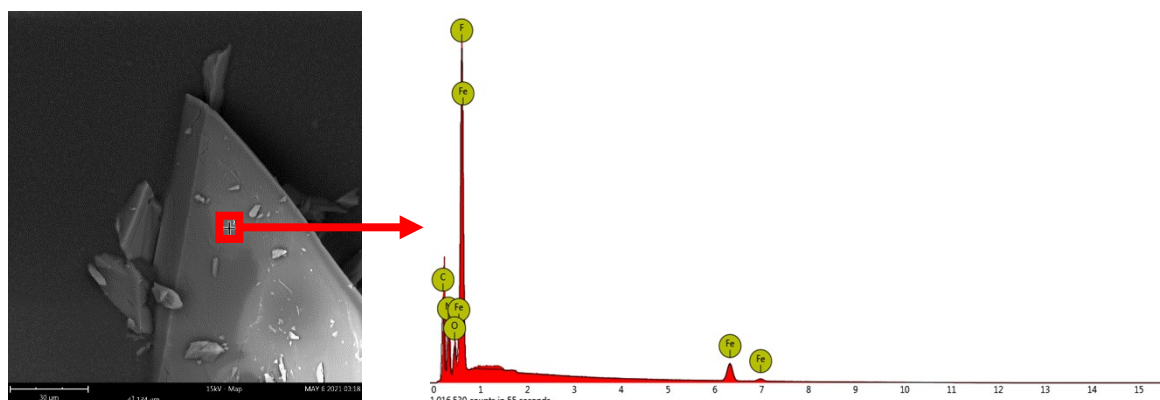


**Figure S5.** SEM image of **1** and corresponding EDS analysis results.

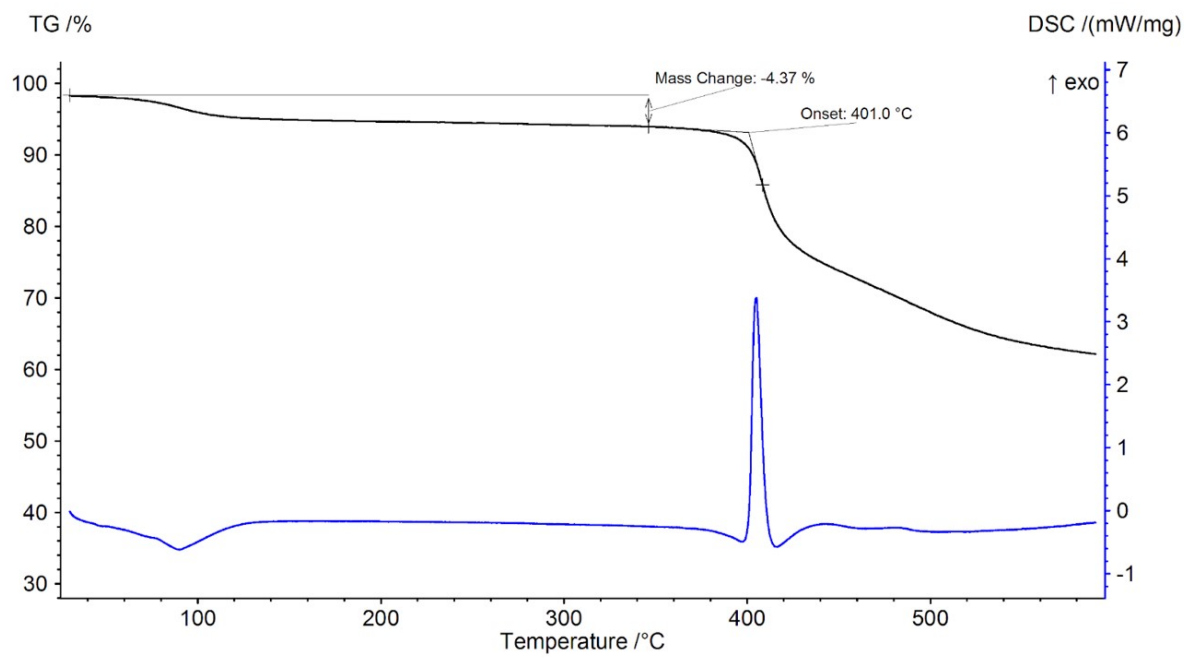


**Figure S6.** Simultaneous thermal analysis plot for  $1 \cdot 6\text{H}_2\text{O}$ .

## S4. Mössbauer, SQUID and LIESST analysis of **1**

### S4.1. Mössbauer analysis of **1**·6H<sub>2</sub>O and desolvated **1**

The Mössbauer experiments at 78 and 298 K for the solvated and desolvated samples demonstrated complete occupancy of the Fe(II) centres in LS-LS state at 78 K and HS-HS at 298 K, corroborating the SQUID results for structures which were allowed to cool slowly (Figure S7). Each of the Mössbauer spectra measured at 78 and 298 K for **1**·6H<sub>2</sub>O and desolvated **1** revealed one quadrupole-split doublet each. At 78 K, **1**·6H<sub>2</sub>O gives rise to a narrow doublet (quadrupole-splitting Q.S. = 0.20 mm s<sup>-1</sup> and isomer shift I.S. = 0.51 mm s<sup>-1</sup>), similar to that for desolvated **1** which displays a narrow doublet (Q.S. = 0.20 mm s<sup>-1</sup> and I.S. = 0.38 mm s<sup>-1</sup>), both of which arise from the LS state. At 298 K, **1**·6H<sub>2</sub>O displays a wide doublet (Q.S. = 0.76 mm s<sup>-1</sup> and I.S. = 0.99 mm s<sup>-1</sup>), as does desolvated **1** (Q.S. = 0.75 mm s<sup>-1</sup> and I.S. = 0.88 mm s<sup>-1</sup>), indicating full occupancy of the HS state.

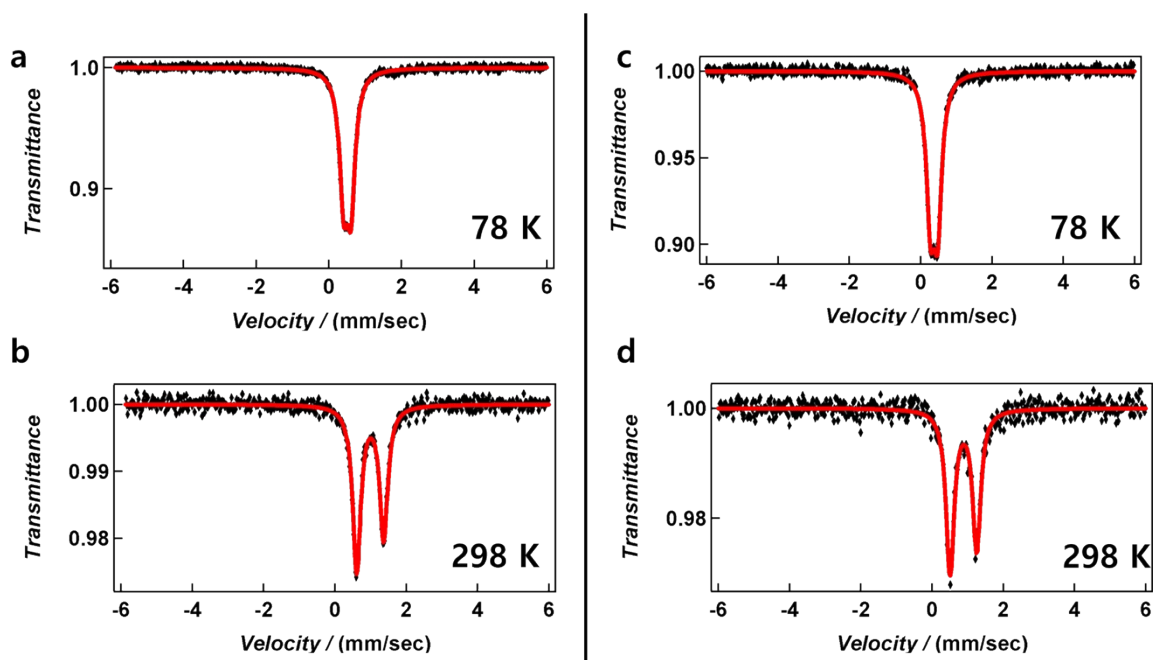
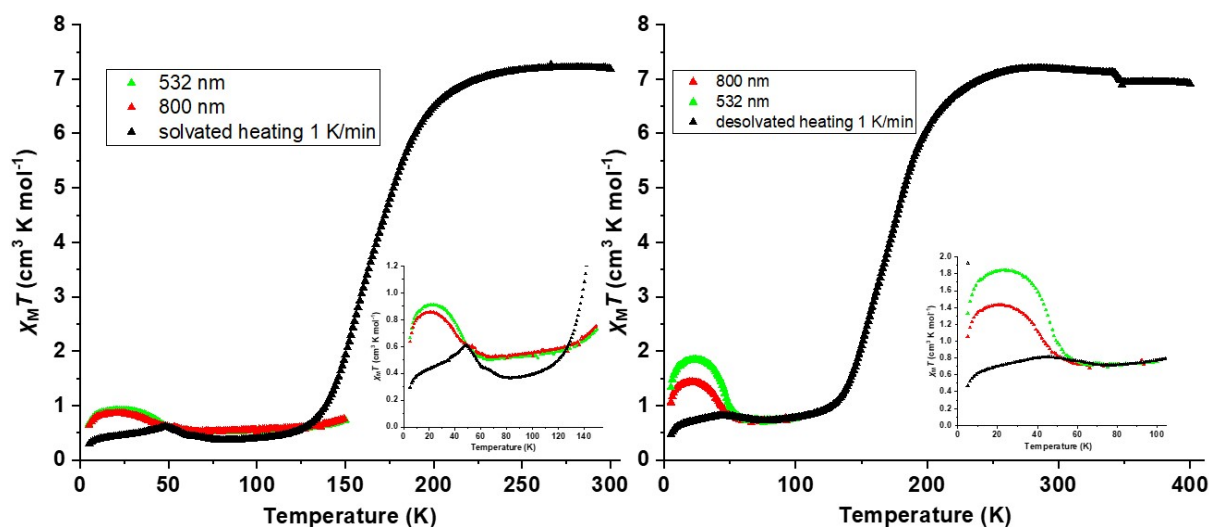


**Figure S7.** Mössbauer spectra of; a) **1**·6H<sub>2</sub>O 78 K, b) **1**·6H<sub>2</sub>O 298 K, c) desolvated **1** at 78 K and d) desolvated **1** at 298 K.

### S4.2. LIESST measurements of **1**·6H<sub>2</sub>O and desolvated **1**

LIESST experiments were carried out for both **1**·6H<sub>2</sub>O and desolvated **1** (Figure S8) to determine the extent of the photoexcitation in response to red (800 nm) and green (532 nm) light. The solvated sample showed a small increase in  $\chi_M T$  for both light sources on irradiation at 5 K. Upon heating following photoexcitation with the red laser, the  $\chi_M T$  value continued to increase up to 0.86 cm<sup>3</sup> K mol<sup>-1</sup> at 21 K, then decreased upon further heating, with a  $T_{\text{LIESST}}$  value of 36 K. The sample's response to the green laser was similar, though more pronounced, rising to a peak of 0.91 cm<sup>3</sup> K mol<sup>-1</sup> at 23 K, with a  $T_{\text{LIESST}}$  value of 42 K. The behaviour of both photoexcited samples beyond the critical temperature were similar, though distinct from the non-photoexcited 1 K min<sup>-1</sup> heating behaviour. Both curves intersect with the peak of the 1 K min<sup>-1</sup> **1**·6H<sub>2</sub>O heating curve at its low temperature peak, before deviating with a higher  $\chi_M T$ . The LIESST curves again intersect the thermal heating curve, but have a later onset of spin transition. This may be evidence that photoexcitation causes a phase change in the solvated

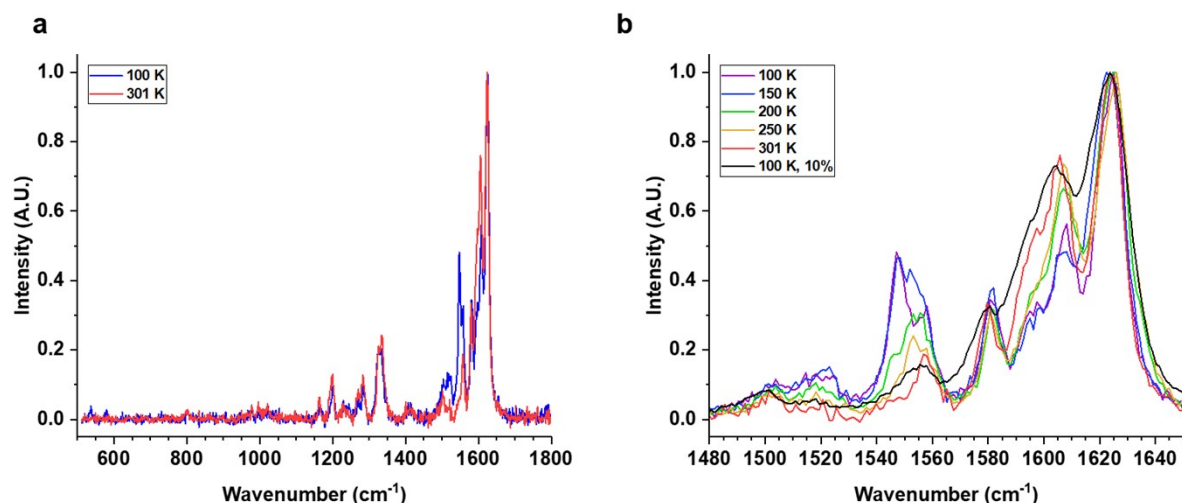
sample, which returns to the HS state via a separate mechanism. LIESST experiments performed on desolvated **1** also displayed a photomagnetic response, with maximum  $\chi_M T$  values of  $1.43 \text{ cm}^3 \text{ K mol}^{-1}$  at 21 K and  $1.84 \text{ cm}^3 \text{ K mol}^{-1}$  at 22 K for red and green light respectively. The  $T_{\text{LIESST}}$  value calculated for green light of 42 K exceeded that found for red light which occurred at 36 K, in the same pattern as that for  $\mathbf{1} \cdot 6\text{H}_2\text{O}$ . Upon further heating, the magnetic susceptibility further decayed, until the curves rejoin the curve of the desolvated **1**  $\text{K min}^{-1}$  heating cycle of **1**.



**Figure S8.** Plot of LIESST results for **1**. a) LIESST results for  $\mathbf{1} \cdot 6\text{H}_2\text{O}$  with the  $1 \text{ K min}^{-1}$  heating cycle shown for reference. b) LIESST results for desolvated **1**, with the  $1 \text{ K min}^{-1}$  heating cycle shown for reference.

## S5. Variable temperature Raman spectroscopy

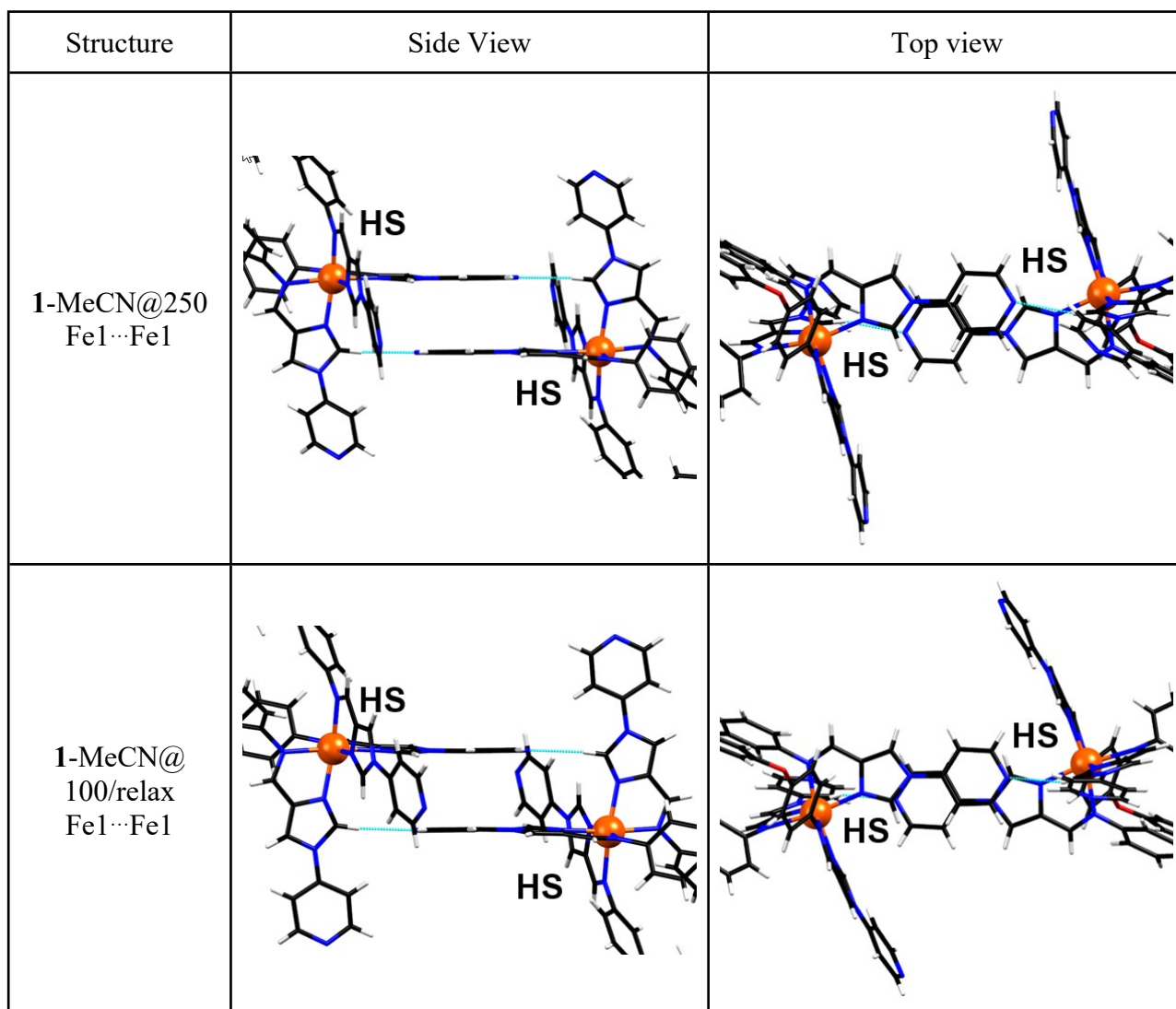
Raman spectroscopy was carried out on  $1 \cdot 6\text{H}_2\text{O}$ , yielding weak data in the region below  $1100\text{ cm}^{-1}$  and significant peaks between  $1100\text{-}1800\text{ cm}^{-1}$  (Figure S9). Vibrations involving the metal ion are typically observed in the region  $100\text{-}1000\text{ cm}^{-1}$ , while peaks arising at  $1000\text{-}2000\text{ cm}^{-1}$  are more likely related to ligand vibrations.<sup>2</sup> At all temperatures, the strongest peak arose at  $1624\text{ cm}^{-1}$ , attributed to N=CH stretching in the imidazole and imine groups. The peak observed at  $1606\text{ cm}^{-1}$  in the 301 K spectrum may be attributed to ring and C-H stretching in the aromatic rings, and the diminishing of this peak with decreasing temperature may indicate less steric freedom for this vibration as the material adopts the LS state. A short peak, consistent with aromatic C=C stretching is observed at  $1557\text{ cm}^{-1}$  at 301 K, which has increased intensity at lower temperatures. An additional peak arises neighbouring this at  $1548\text{ cm}^{-1}$  at 150 K and 100 K, providing a clear marker of the LS state, and may be attributed to the same vibrational mode, altered by transition to the LS state. After cooling to 100 K, a measurement was performed using 10% laser power (8.9 mW), which provided a spectrum more consistent with that measured at 301 K than 100 K, indicating that photoexcitation brings about the metastable HS state observed in LIESST studies (Figure S8).

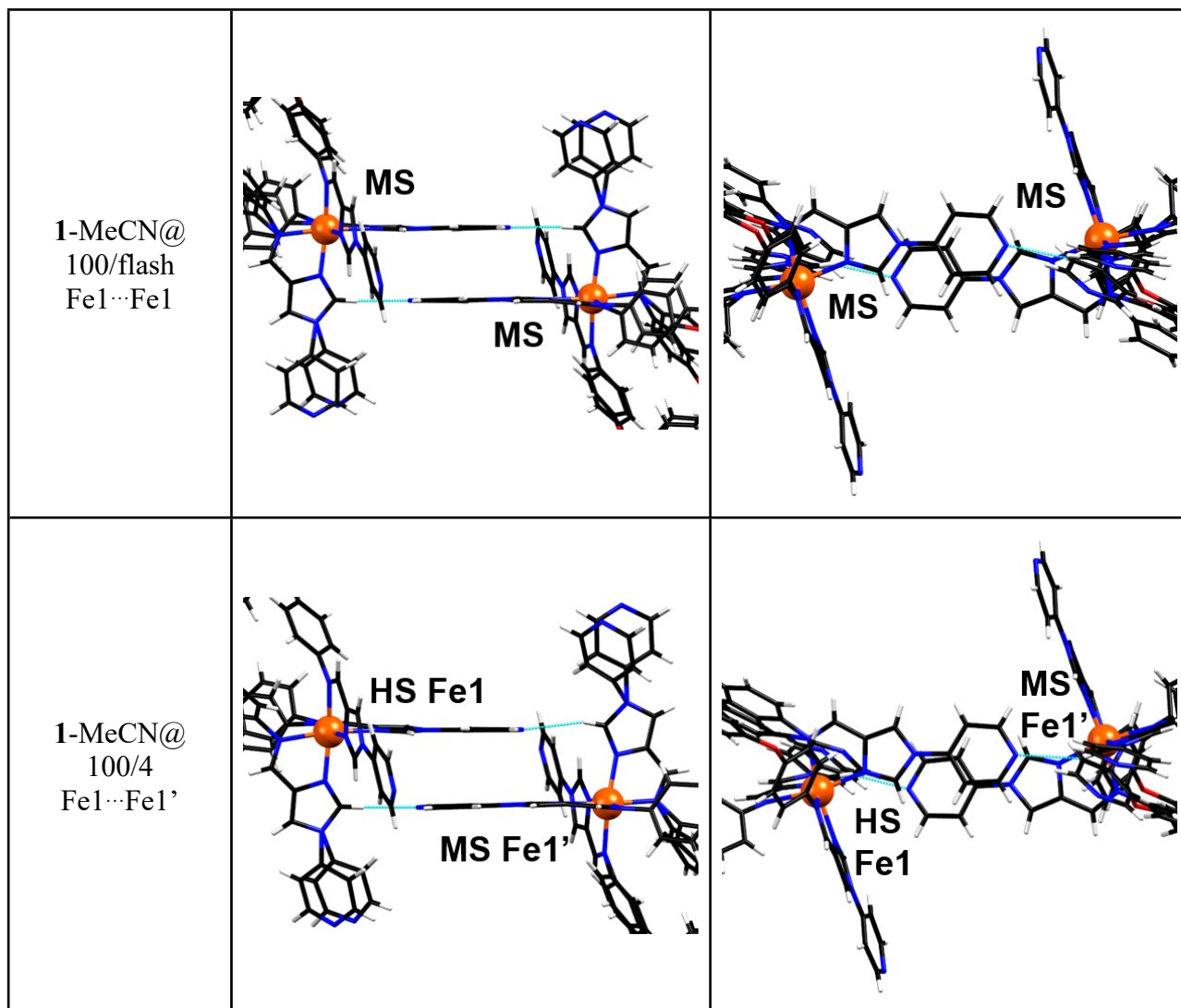


**Figure S9.** Variable temperature Raman data for  $1 \cdot 6\text{H}_2\text{O}$  at the cooling rate of  $1\text{ K min}^{-1}$ . a) Full spectral width at 100 K (blue) and 301 K (red). b) Close-up of the region  $1480\text{-}1650\text{ cm}^{-1}$ , which showed the most variation across the temperature series. 1% laser power (0.89 mW) was used to collect spectra at 300 K (red), 250 K (orange), 200 K (green), 150 K (blue), 100 K (purple), and 10% laser power (8.9 mW) was used at 100 K (black) to cause the LIESST effect.

## S6. Intermolecular interactions of 1-MeCN

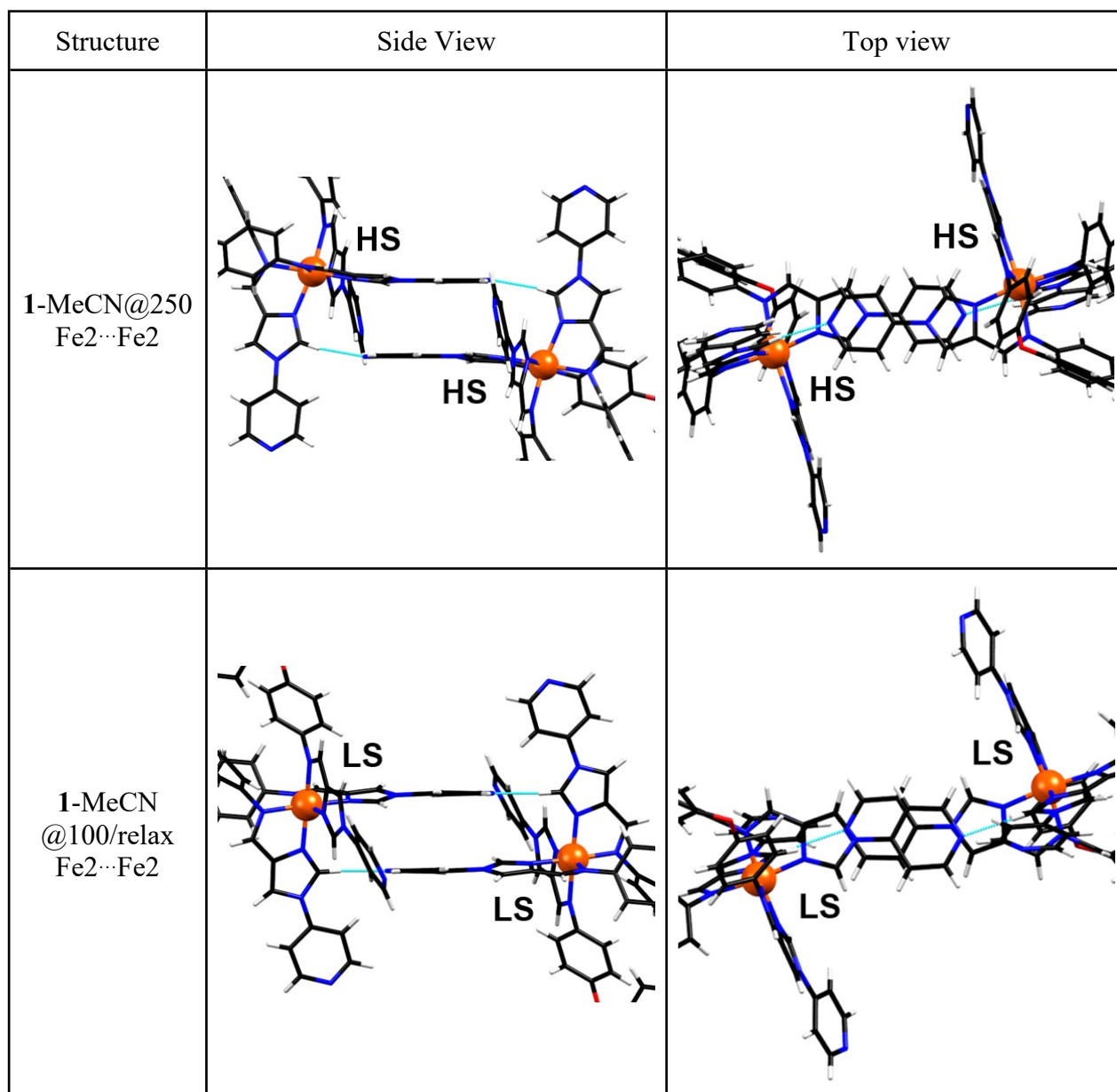
**Table S4.** Contacts along the 1D chain formed by the terminal pyridine groups of ligand A at the Fe1 end of the helicate. These contacts join helicates of opposite chirality through  $\pi$ - $\pi$  stacking between A pyridines and N $\cdots$ HC hydrogen bonds between pyridyl N atoms and imidazole CH groups of ligand C.

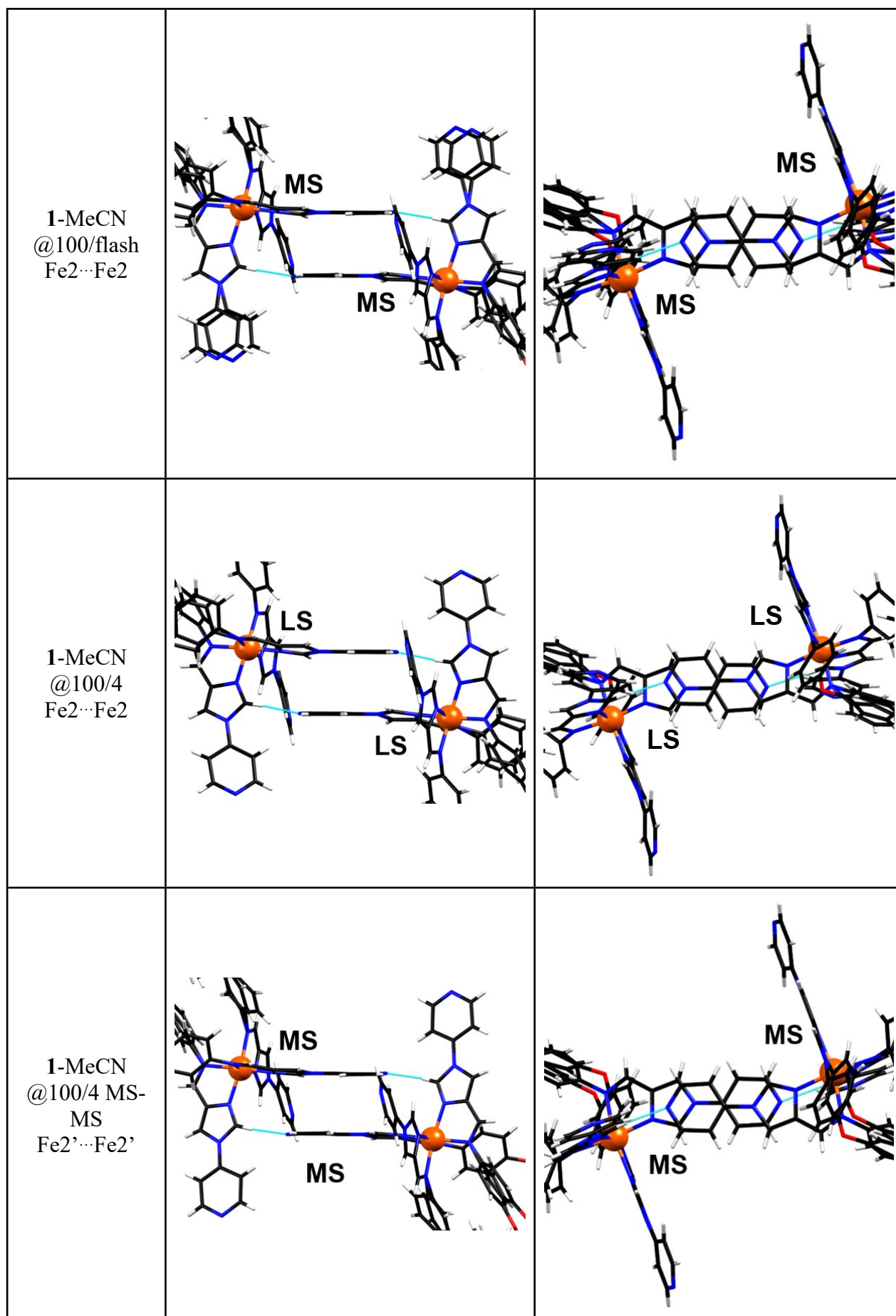




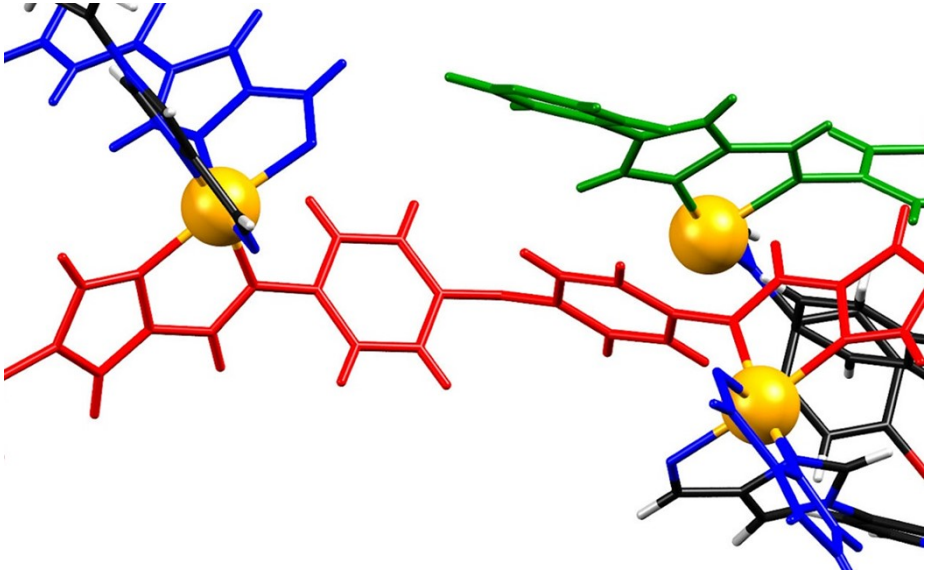
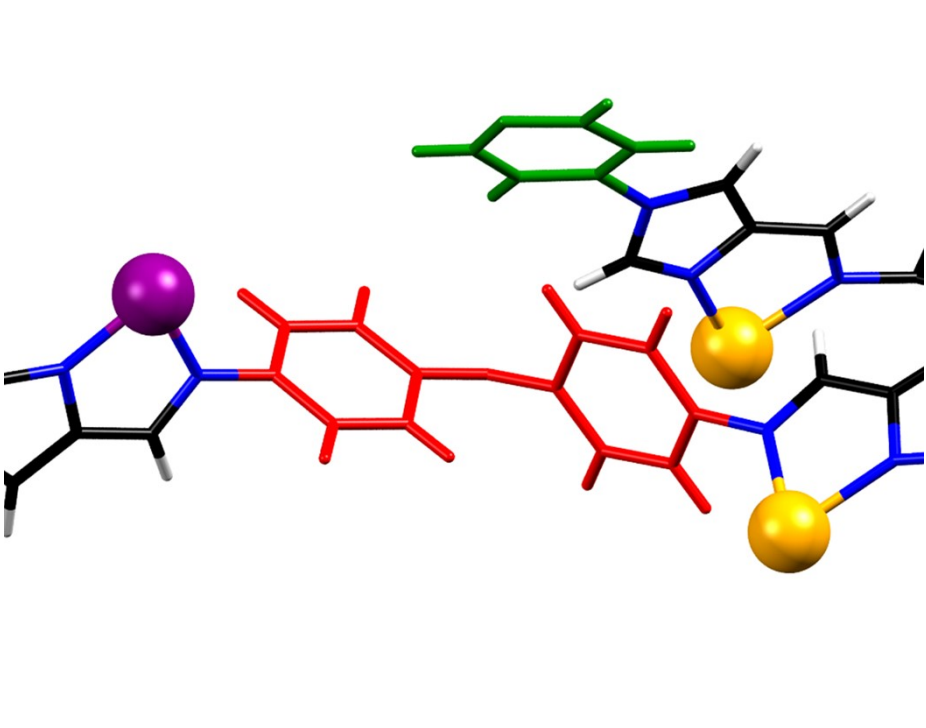


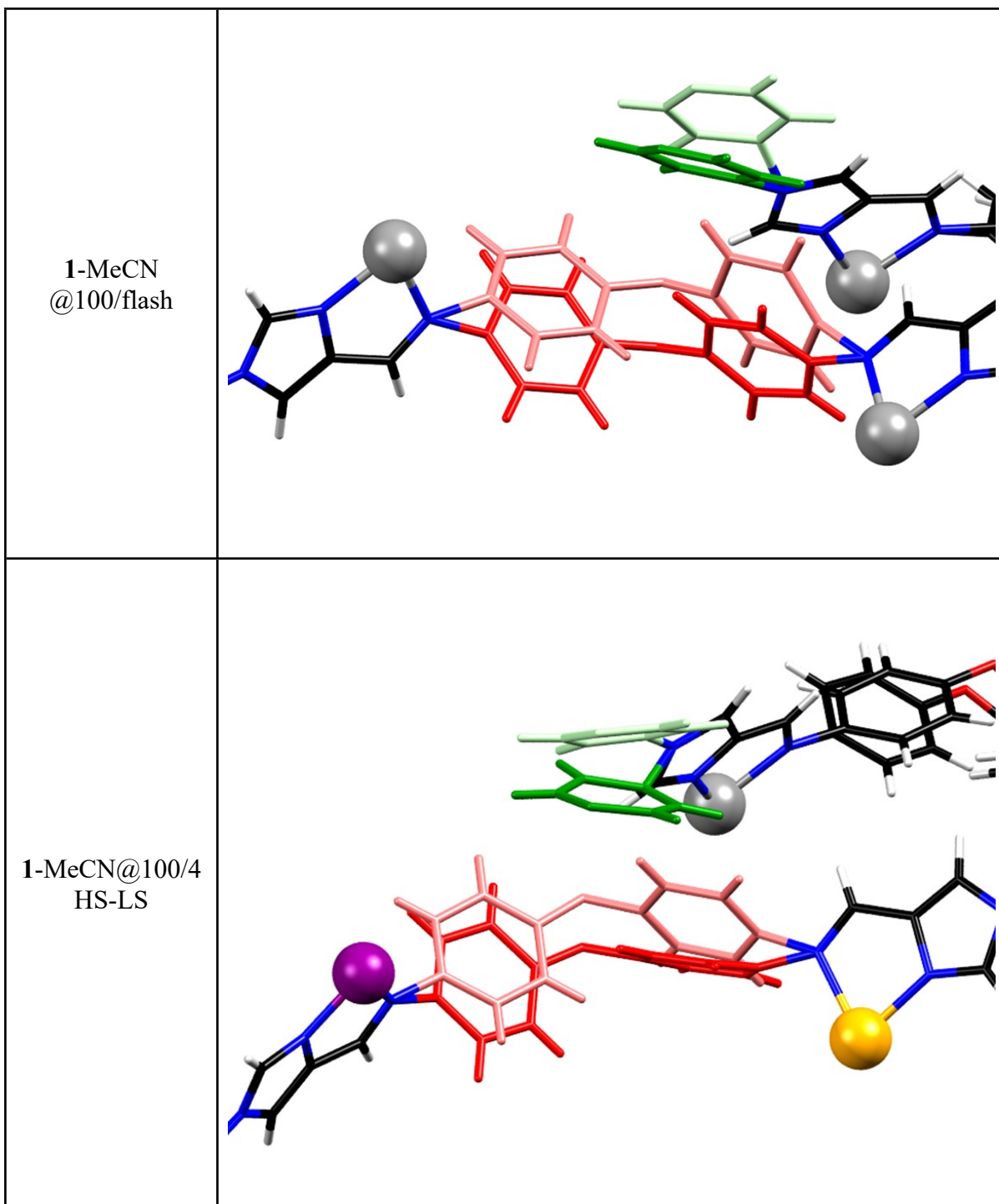
**Table S5.** Contacts along the 1D chain formed by the terminal pyridine groups of ligand **A** at the Fe2 end of the helicate. These contacts join helicates of opposite chirality through  $\pi$ - $\pi$  stacking between **A** pyridines, and N $\cdots$ HC hydrogen bonds between pyridyl N atoms and imidazole CH groups of ligand **B**.



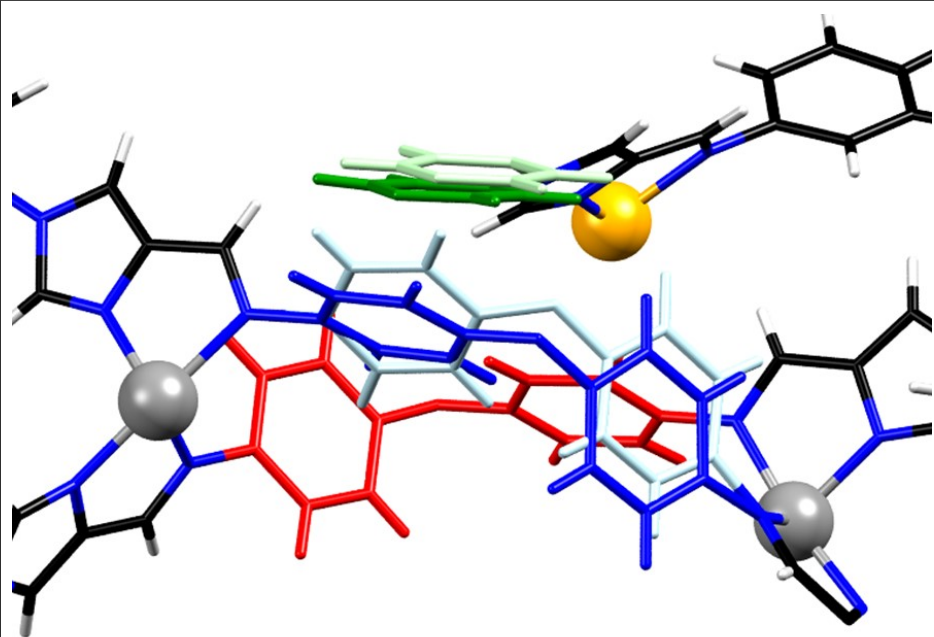


**Table S6.** Contacts between the linker segment of ligand **A** and the terminal pyridine of ligand **C** on an adjacent helicite. Ligand **A** is shown in red, **B** in blue and **C** in green, with secondary disordered parts shown in lighter colours. HS Fe centres are shown in orange, LS Fe in purple and MS Fe in grey.

Structure	A linker to C pyridine contact
1-MeCN@250	 <p>The image shows a molecular structure with a central red linker segment. To its left, a blue pyridine ring is coordinated to a yellow HS Fe center. To its right, a green pyridine ring is coordinated to another yellow HS Fe center. The linker segment is shown in red, and the pyridine rings are in blue and green. The structure is shown in a perspective view, highlighting the spatial arrangement and potential interactions between the linker and the pyridine rings.</p>
1-MeCN @100/relax	 <p>The image shows a molecular structure similar to the one above, but with a different arrangement. The central red linker segment is shown in red. To its left, a purple LS Fe center is coordinated to a blue pyridine ring. To its right, a yellow HS Fe center is coordinated to a blue pyridine ring. The structure is shown in a perspective view, highlighting the spatial arrangement and potential interactions between the linker and the pyridine rings.</p>



1-MeCN@100/4  
MS-MS



## S7. Scaling of crystal packing coefficient and molecular volume.

Crystal packing coefficient and molecular volume calculations were carried out in Olex2.<sup>3</sup> For structures exhibiting no disorder, the calculation was straightforward, and performed with a selection of all atoms in the helicate structure including H atoms. Where orientational disorder was present, using the same simple method will artificially increase the value of each result, since occupancies of various parts are not accounted for. To amend this, all atoms in the helicate designated part 0 and part 1 (0/1) were selected, then the volume and density parameters were recorded. The same process was repeated for part 0 and part 2 (0/2) atoms. The volume of the [0/1] and [0/2] helicates were scaled by the occupancies of all disordered moieties, according to:

$$occ(P1) = \frac{[occ(M1, P1) + occ(M2, P1) + \dots + occ(Mi, P1)]}{[occ(M1, P1) + occ(M2, P1) + \dots + occ(Mi, P1)] + [occ(M1, P2) + occ(M2, P2) + \dots + occ(Mi, P2)]}$$

$$occ(P2) = \frac{[occ(M1, P2) + occ(M2, P2) + \dots + occ(Mi, P2)]}{[occ(M1, P1) + occ(M2, P1) + \dots + occ(Mi, P1)] + [occ(M1, P2) + occ(M2, P2) + \dots + occ(Mi, P2)]}$$

Where:

$occ(P1)$  and  $occ(P2)$  denote the scaled occupancies of [0/1] and [0/2] respectively

$occ(Mi, P1)$  and  $occ(Mi, P2)$  refer to the occupancies of the  $i$ th disordered moiety on parts 1 and 2 respectively.

The final value for each parameter (Y) was calculated by:

$$Y = [occ(P1) \times Y(0/1)] + [occ(P2) \times Y(0/2)]$$

## S8. Helicate structural parameters.

In order to quantify the reorientation of key parts of the dinuclear triple helicate units, and examine the correlative effects between molecular reconfiguration and the crystal structure of **1**-MeCN, several structural parameters have been examined, similar to our previous work.<sup>4-6</sup> Linker ring torsions (S8.1) were used to describe the orientations of the benzene groups within the linker moieties of each ligand. Pitch and yaw angles (S8.2) were taken in mutually orthogonal projections for each chelate ring in the structure, describing the side-to-side twisting and the back-and-forth rocking of each chelate group relative to the interhelical axis. Additionally, the deviation between the interhelical axis the terminal pyridine moieties (secondary bond axis, S8.3) was used to show to what degree the terminal groups are spread. This suite of geometric parameters allows for the determination of molecular dynamics related to SCO, and correlation with lattice parameters can be used to show how molecular reconfigurations and phase changing dynamics are entwined.

The helicate can be divided into components, with the orientation of each component used to provide insight into the overall conformation achieved by different parts of each ligand. The linker moieties were modelled using linker torsion (S8.1), which indicates the degree of twist of each of the benzene rings, relative to a reference plane describing the linker segment overall. The angle between the intermetallic axis and the axis defined by the two coordinating N atoms in each chelate ring can be taken, and this was further deconstructed into pitch and yaw angles to more specifically indicate the direction of the reorientations in the chelate groups. By a similar methodology, angles between the intermetallic axis and the secondary bond axes were calculated. Here, the secondary bond axis refers to the interval between N atoms in terminal pyridines, and the C atoms opposite in the ring (N1 - C3 or N8 - C28), which reflects the direction in which a coordinate bond from the secondary donor sites may form with respect to the intermetallic axis (S8.3). This allows for quantification of the degree of spreading of the terminal pyridyl groups. Since the coordinating imidazoleimine and the terminal pyridine are both rigid groups, the spread of the secondary bond axes is closely linked to the orientation of the internal chelating section of the ligand. All of these parameters are defined such that they refer to an internal structural feature for consistent comparison; either the intermetallic axis, or in the case of linker ring torsions, a reference plane describing the linker orientation.

Following analysis of the structural measurements (Table S7) we are able to suggest a mechanism by which slow cooling allows the lattice of **1** to undergo a transition to [HS-LS] in the full population of helicate molecules in the solid, while faster cooling inhibits this transformation. Several ligand reconformations are demonstrated in the **1**-MeCN@100/relax structure, which differ significantly from the 250 K structure (Table S7). One key feature is that the linker segment of ligand **A** repositions with a transition of Fe2 to LS. This occurs due to the rearrangement of the chelate group of **A** at Fe2, which changes the pitch to negative, and causes the benzene rings in **A** to exchange torsion values (Table S7). This, along with motion towards the terminal **C** pyridyl at Fe1 of an adjacent helicate, may induce a transition of the adjacent Fe1 to LS, due to the semi-rigid connection between the terminal pyridine and chelating imidazoleimine. This is demonstrated in the kinetically trapped **1**-MeCN@100/4 structure through the low Fe1' octahedral distortion parameters. Additionally, the rearrangement of the **C** imidazole group skews the orientation of the CH group associated with the terminal N...HC hydrogen bond, weakening the contact between Fe1 centres along the 1D chains, which may contribute to the loss of inversion symmetry across these sites (Table S4). In the fully relaxed structure, further reorientation in ligand groups puts into effect an overall supramolecular rearrangement. Transitioning the bulk of helicates in the solid to the [HS-LS] state instigates a significant decrease in the magnitude of **B** pitch at both ends of the helicate

which allows terminal pyridyl groups of **B** to draw inwards and lower the secondary bond axis values of **B**. This in turn leads to the compression of 1D chains towards each other along the *b*-axis.

**Table S7.** Selected geometric parameters describing the orientations of helicate components. 1 K min<sup>-1</sup> values are shown to compare with those obtained at the extreme ends of the temperature range.

Structure (1-MeCN@...)	*A torsion <sup>a</sup> (°)	A Pitch <sup>b</sup> (°)	A Yaw <sup>c</sup> (°)	B Pitch <sup>b</sup> (°)	B Yaw <sup>c</sup> (°)	*A Secondary bond axis <sup>d</sup> (°)	*B Secondary bond axis <sup>d</sup> (°)
<b>100/relax</b>	<b>Fe1:</b> 61.7, <b>Fe2:</b> 32.8	<b>Fe1:</b> 6.9, <b>Fe2:</b> -2.8	<b>Fe1:</b> 33.4, <b>Fe2:</b> 33.0	<b>Fe1:</b> 4.9, <b>Fe2:</b> -0.8	<b>Fe1:</b> 34.0, <b>Fe2:</b> 38.0	<b>Fe1:</b> 44.0, <b>Fe2:</b> 44.2	<b>Fe1:</b> 32.4, <b>Fe2:</b> 46.1
<b>100/flash</b>	<b>Fe1:</b> 45.8, <b>Fe2:</b> 50.5	<b>Fe1:</b> 3.2, <b>Fe2:</b> 1.6	<b>Fe1:</b> 32.5, <b>Fe2:</b> 34.5	<b>Fe1:</b> 6.76, <b>Fe2:</b> -2.9	<b>Fe1:</b> 33.2, <b>Fe2:</b> 35.7	<b>Fe1:</b> 42.6, <b>Fe2:</b> 51.8	<b>Fe1:</b> 42.4, <b>Fe2:</b> 48.4
<b>100/1</b>	<b>Fe1:</b> 40.4, <b>Fe2:</b> 57.0	<b>Fe1:</b> 1.9, <b>Fe2:</b> 1.3	<b>Fe1:</b> 33.1, <b>Fe2:</b> 35.1	<b>Fe1:</b> 6.3 <b>Fe2:</b> -2.1	<b>Fe1:</b> 33.4, <b>Fe2:</b> 34.8	<b>Fe1:</b> 42.7, <b>Fe2:</b> 51.5	<b>Fe1:</b> 43.3, <b>Fe2:</b> 47.4
<b>150/1</b>	<b>Fe1:</b> 35.7, <b>Fe2:</b> 59.6	<b>Fe1:</b> 2.2, <b>Fe2:</b> 1.3	<b>Fe1:</b> 32.3, <b>Fe2:</b> 35.2	<b>Fe1:</b> 6.7, <b>Fe2:</b> -1.9	<b>Fe1:</b> 33.1, <b>Fe2:</b> 35.2	<b>Fe1:</b> 42.7, <b>Fe2:</b> 52.0	<b>Fe1:</b> 43.1, <b>Fe2:</b> 48.4
<b>200/1</b>	<b>Fe1:</b> 31.5, <b>Fe2:</b> 60.0	<b>Fe1:</b> 2.2, <b>Fe2:</b> 2.6	<b>Fe1:</b> 31.6, <b>Fe2:</b> 35.4	<b>Fe1:</b> 8.8, <b>Fe2:</b> -4.4	<b>Fe1:</b> 33.3, <b>Fe2:</b> 34.1	<b>Fe1:</b> 43.2, <b>Fe2:</b> 53.8	<b>Fe1:</b> 43.5, <b>Fe2:</b> 52.7
<b>250</b>	<b>Fe1:</b> 31.1, <b>Fe2:</b> 60.0	<b>Fe1:</b> 2.3, <b>Fe2:</b> 2.5	<b>Fe1:</b> 31.7, <b>Fe2:</b> 35.6	<b>Fe1:</b> 8.6, <b>Fe2:</b> -4.2	<b>Fe1:</b> 33.4, <b>Fe2:</b> 34.0	<b>Fe1:</b> 43.5, <b>Fe2:</b> 54.2	<b>Fe1:</b> 43.5, <b>Fe2:</b> 52.4

<sup>a</sup> The linker torsion angle measured from planes of each benzene group linked to a reference plane, identifying the degree of twist the linker region adopts at each end of the helicate.

<sup>b</sup> Pitch specifies the back and forth rocking orientation of the chelate groups in relation to the intermetallic axis.

<sup>c</sup> Yaw specifies the side-to-side twisting orientation of the chelate rings relative to the intermetallic axis.

<sup>d</sup> The secondary bonding axis measures the orientation of the terminal pyridine groups with respect to the intermetallic axis.

\* In structures exhibiting orientational disorder, the parameter values were calculated for each part, and those values were scaled by the occupancy of the respective part and summed to provide the stated value.

### S8.1. Linker torsion

The linker ring torsion angle can be calculated for each benzene ring separately for each linker segment. First, a reference plane outlining the linker (C10-O1-C19) was calculated for each ligand (Figure S10a). Then the planes of each aromatic ring attached to O1 (C10-C15; C16-C21) were calculated. The angle between the reference plane and each aromatic plane were taken (Figure S10b), which is indicative of the degree to which the benzene rings are twisted with respect to the overall linker segment.



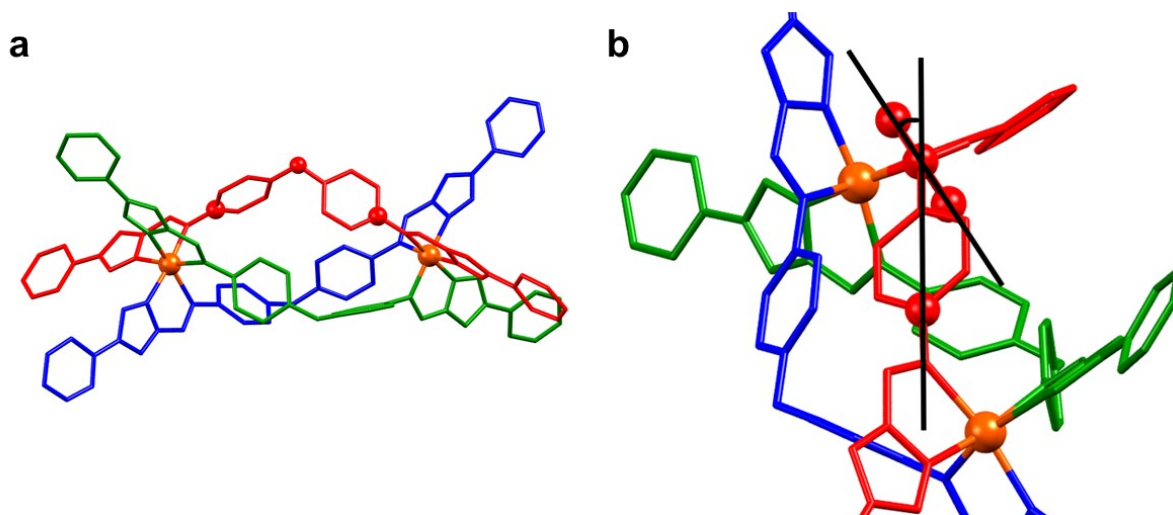


**Figure S10.** Schematic representing the linker torsion angle. a) The atoms selected (shown as balls) to define the reference plane (C9-O1-C19). b) The measured angle for the linker torsion with respect to the reference plane.

### S8.2. Pitch and yaw

The angle between the chelate ring and intermetallic axis can be deconstructed into two components, representing the back and forth rocking (pitch, Figure S11a,b) and side to side twisting (yaw, Figure S11c) of each chelate ring, relative to the intermetallic axis. In order to quantify these motions, we adapted the concepts of pitch, roll and yaw, such that the combination of each angular component uniquely described the orientation of each chelate ring relative to the intermetallic axis. The angle between the intermetallic axis is taken in two orthogonal two-dimensional projections, providing the pitch and yaw values of each of the six chelate rings in the helicate.

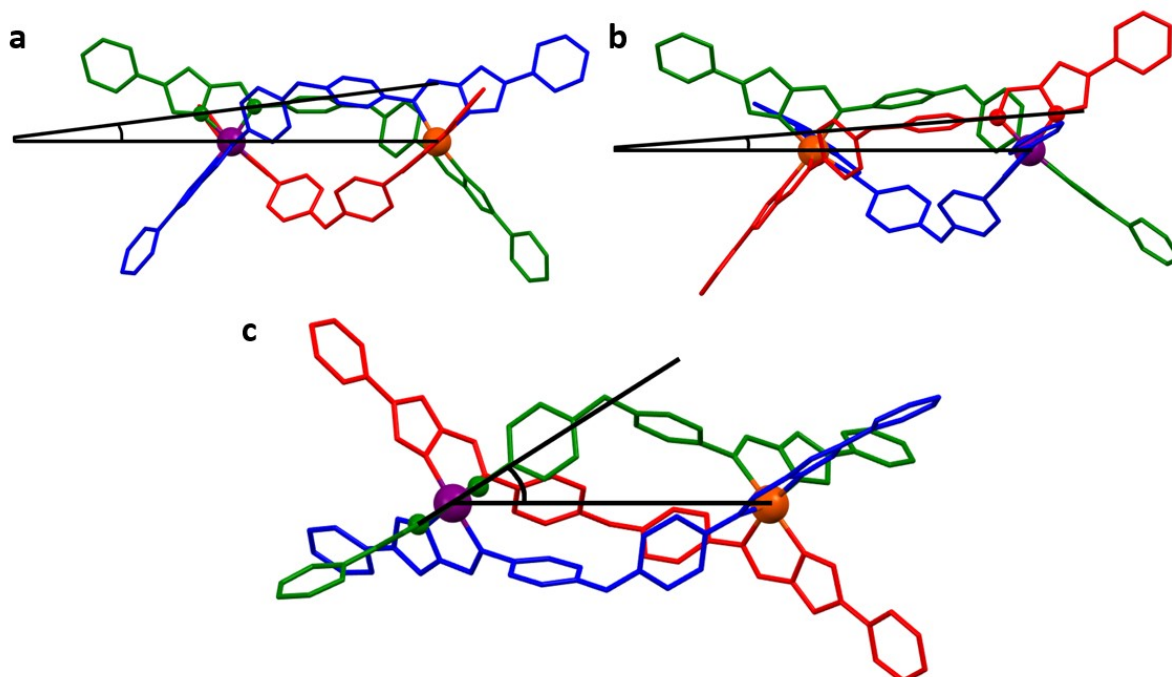


**Figure S11.** Schematics demonstrating a) the pitch angle for each chelate ring, in this case the pitch is positive, b) an example of negative pitch, c) the yaw angle for chelate rings.

After taking the coordinates of  $Fe_i$ ,  $Fe_j$ ,  $N_i$  and  $N_j$ , we subject them to the following procedure to calculate the pitch and yaw angular components.

- All coordinates were translated such that  $Fe_i$  occupied the origin.
- The cross product of vectors  $N_i$  and  $N_j$  was calculated.
- All coordinates rotated about the  $x$ -axis, such that the cross product lay in the  $xz$  plane.
- All coordinates were rotated about the  $y$ -axis, such that the cross product lay on the  $z$ -axis. This in turn means that  $N_i$  and  $N_j$  both lie in the  $xy$  plane.
- All coordinates were rotated about the  $z$ -axis, such that  $Fe_j$  lay in the  $xz$  plane.
- Yaw was calculated using the  $Fe_j$   $z$  and  $x$  coordinates by  $\arctan(z/x)$ .
- Pitch was calculated using the gradient of the  $N_i - N_j$  interval by  $\arctan((N_j y - N_i y) / (N_j x - N_i x))$ .

The signs of all yaw values were taken as positive, and the signs of pitch values were checked using the ratios of the  $y$  coordinates of  $N_j$  and  $N_i$  to determine the sign. Positive pitch was taken to mean the coordinating  $N$  in the imidazole lay closer to the intermetallic axis than the coordinating  $N$  of the imine, and the opposite is true in the case of negative pitch (Figure S11 a, b).

Since we are using a simplistic model, involving only the coordinating  $N$  atoms, we assume that the roll component is negligible i.e. the five-membered chelate ring is close to planar. Calculating the angle between the chelate interval and intermetallic axis in 2D projection orthogonal to those used for pitch and yaw arbitrarily returns the value of  $90^\circ$ .

### S8.3. Chelate ring angles and bond axis

In order to relate the motion of each ligand to distortions about each coordination centre, the angle between the vector defining each chelate ring ( $N_3-N_4$ ;  $N_6-N_5$ ) and the intermetallic axis ( $Fe_1-Fe_2$ ) was calculated.

The angle between each chelate ring and the intermetallic axis was calculated by a similar method to our previous work.<sup>4,5</sup> The coordinates of  $Fe_i$ ,  $Fe_j$  and two  $N$  atoms defining a chelate ring ( $N_i$  and  $N_j$ ) were taken. These coordinates were transformed by several operations as follows:

- All four points were translated by the same distance, such that  $Fe_i$  occupied the origin of the Cartesian system.
- Atoms  $N_i$  and  $N_j$  were translated by the same distance, such that  $N_i$  sat at the origin.
- All coordinates were rotated about the  $z$ -axis, such that the  $Fe_j$  sat in the  $xz$  plane.
- All coordinates were rotated about the  $x$ -axis, such that  $Fe_j$  sat on the  $z$ -axis.
- All coordinates were rotated about the  $z$ -axis, such that  $N_j$  sat in the  $yz$  plane. The angle between the chelate ring and the intermetallic axis was then calculated using the  $N_j$  coordinates by  $\arctan(y/z)$ .

The same methodology was used to quantify the spread of terminal pyridyl groups. In these calculations, the coordinates of the chelating N's were substituted with the pyridyl N and the opposite C in the same pyridine.

## S9. PXRD

### S9.1. PXRD Patterns

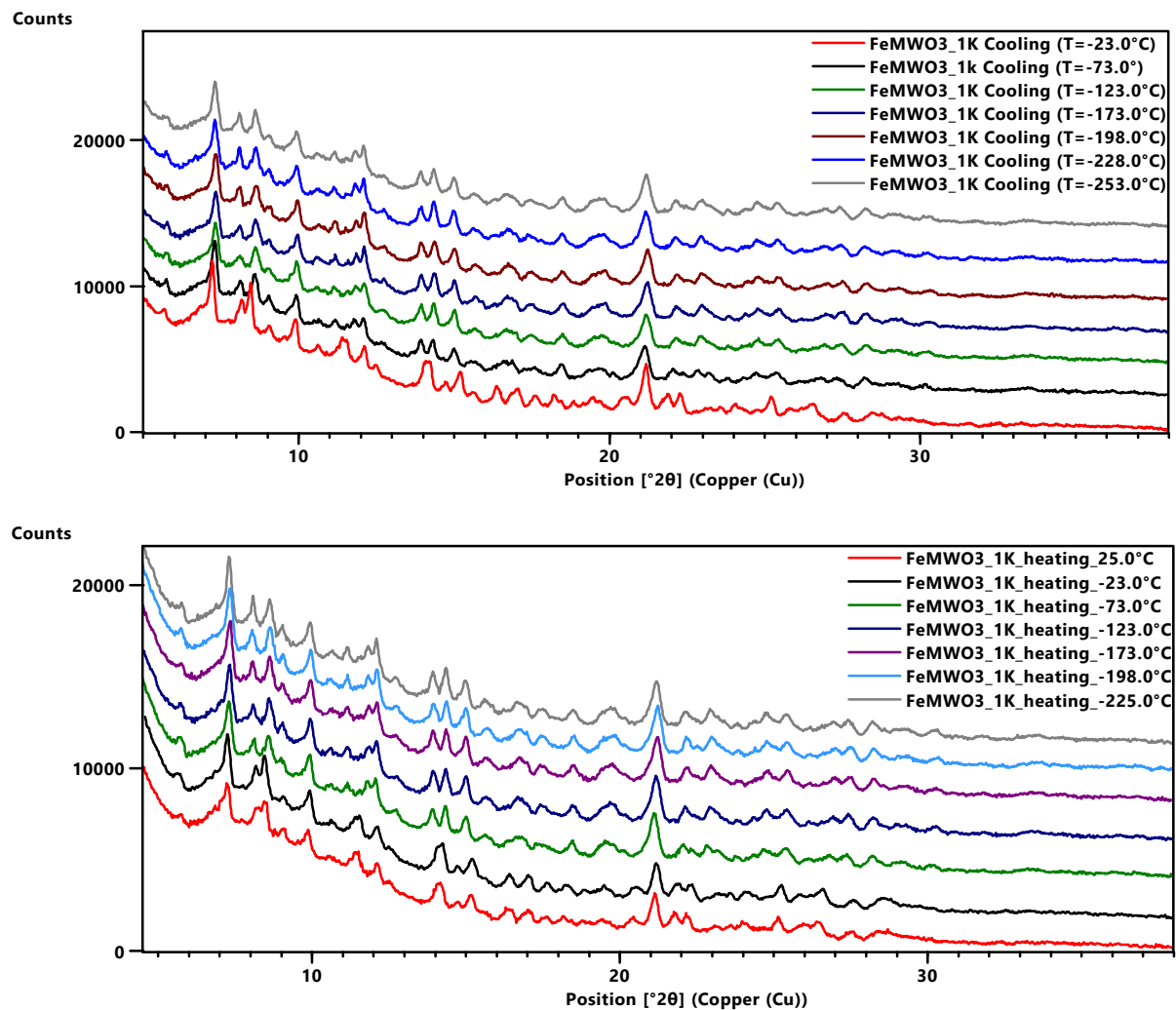


**Figure S12.** PXRD patterns of the  $1 \cdot 6\text{H}_2\text{O}$  at different temperatures and heating with  $1 \text{ K min}^{-1}$  cooling (top) and heating (bottom). The y-axis is scale adjusted to generate the stack plot. The peak at  $\sim 14^\circ 2\theta$  starts showing a split at after  $-73^\circ\text{C}$ .

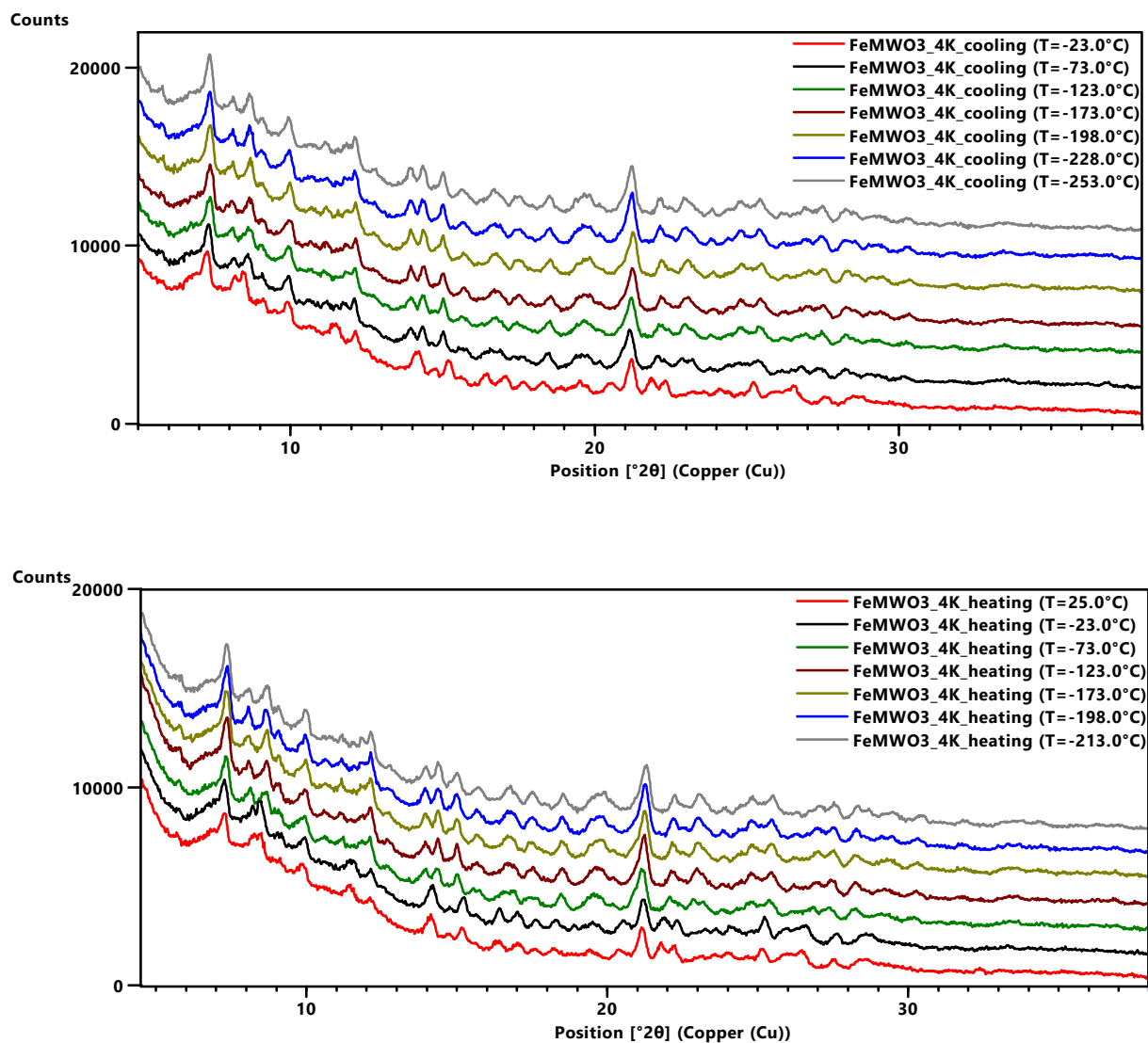


**Figure S13.** PXRd patterns of the  $1 \cdot 6\text{H}_2\text{O}$  at different temperatures and heating with  $4 \text{ K min}^{-1}$  cooling (top) and heating (bottom). The y-axis is scale adjusted to generate the stack plot. The peak at  $\sim 14^\circ 2-\theta$  starts showing a split at after  $-73^\circ\text{C}$ .

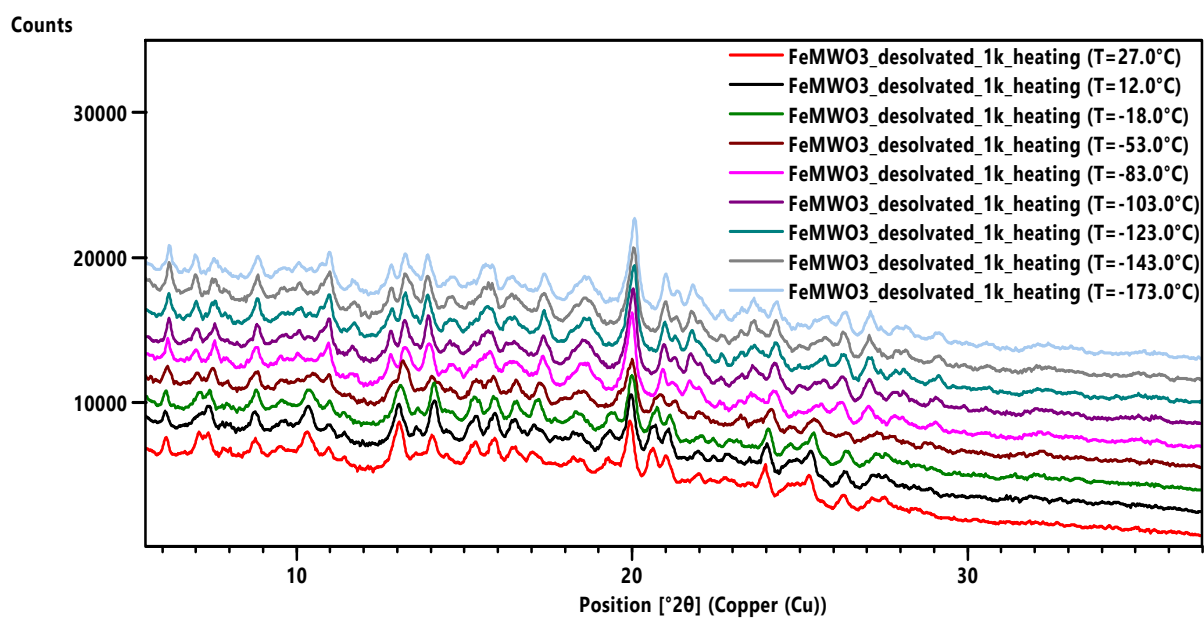
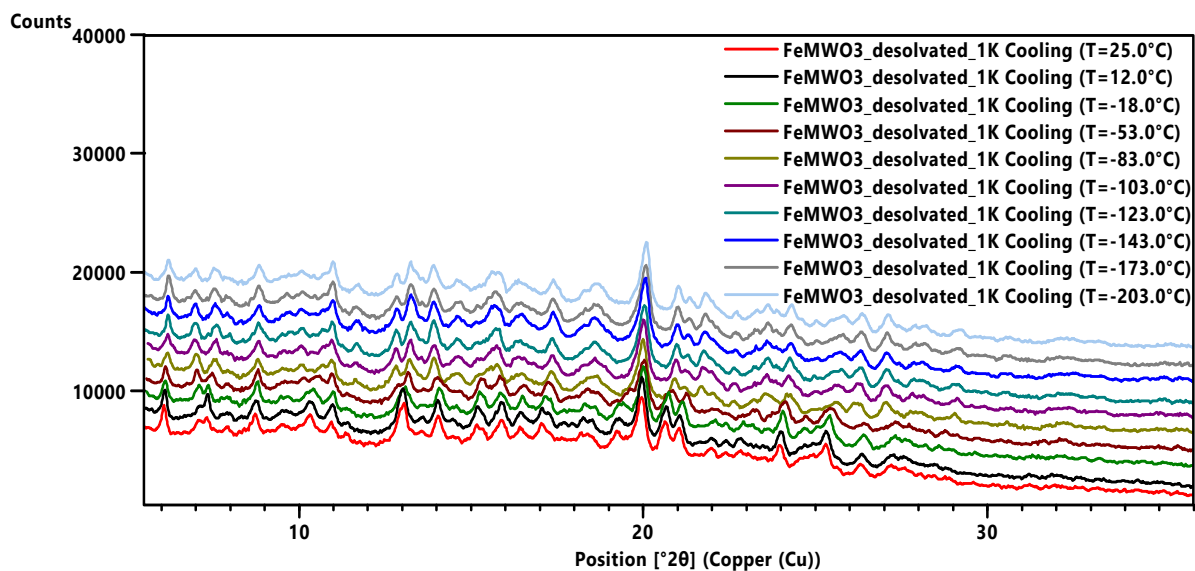


**Figure S14.** PXRD patterns of desolvated **1** at different temperatures with 1 K min<sup>-1</sup> cooling (top) and heating (bottom). The y-axis is scale adjusted to generate the stack plot.

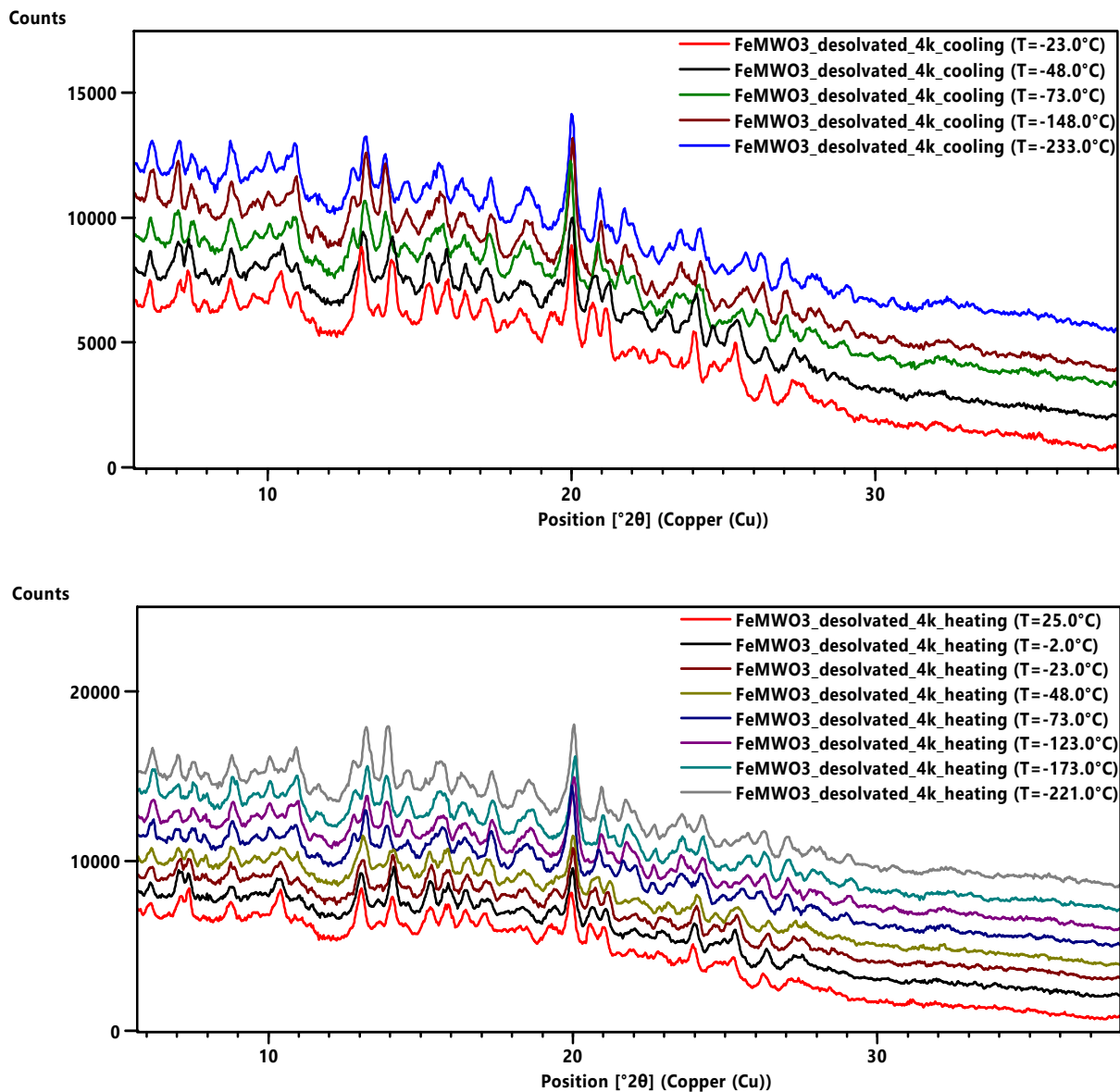


**Figure S15.** PXRD patterns of desolvated **1** at different temperatures with 4 K min<sup>-1</sup> cooling (top) and heating (bottom). The y-axis is scale adjusted to generate the stack plot.

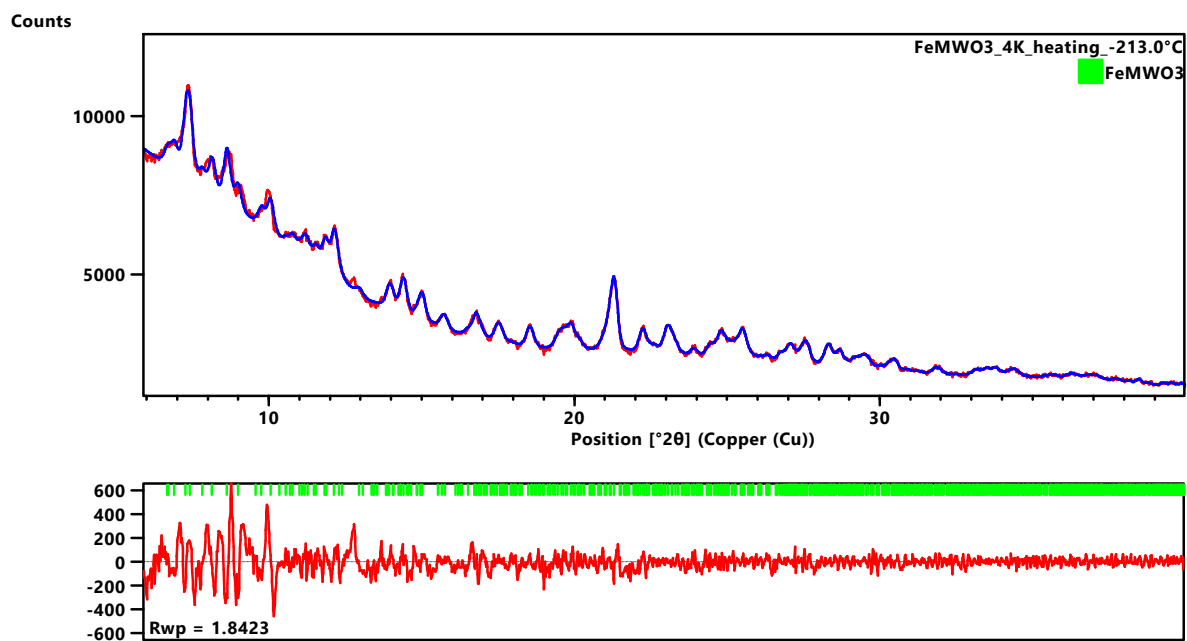


**Figure S16.** Full pattern Pawley fit plot at 60 K with 4 K min<sup>-1</sup> heating rate. Plot above is overlay of experimental (red) and calculated (blue) pattern. Plot below is difference plot.



## S9.2. PXRD scan-rate dependent spectral differences

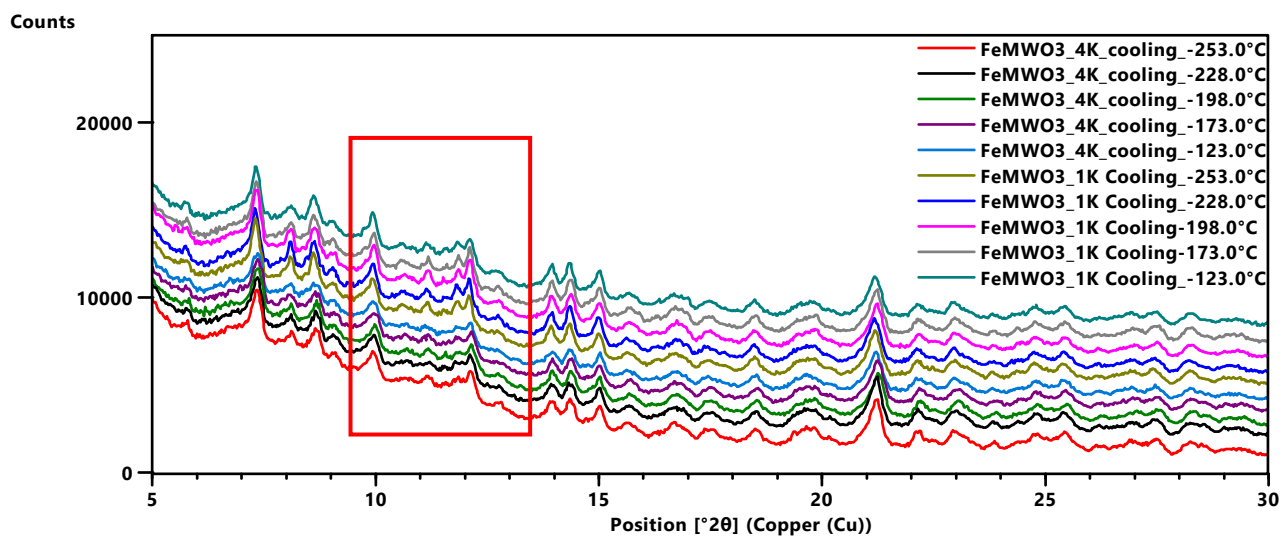


**Figure S17.** Comparison of powder patterns of  $1 \cdot 6\text{H}_2\text{O}$  at  $1 \text{ K min}^{-1}$  and  $4 \text{ K min}^{-1}$  cooling rates. The main region of difference is highlighted in the red box.

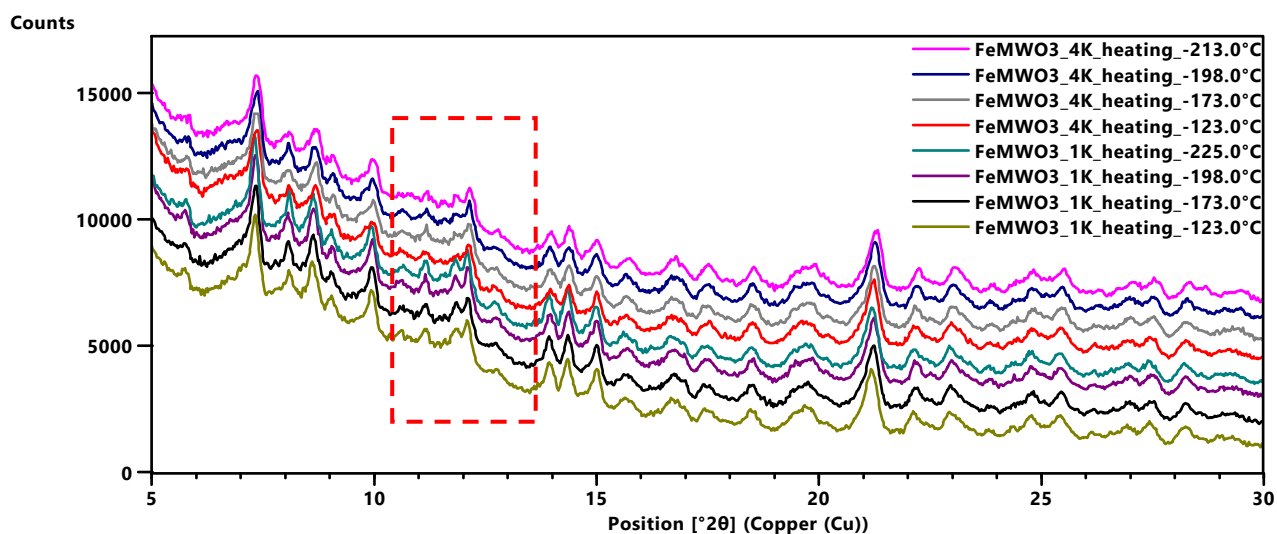


**Figure S18.** Comparison of powder patterns of  $1 \cdot 6\text{H}_2\text{O}$  at  $1 \text{ K min}^{-1}$  and  $4 \text{ K min}^{-1}$  heating rates. The main region of difference is highlighted in the red box.

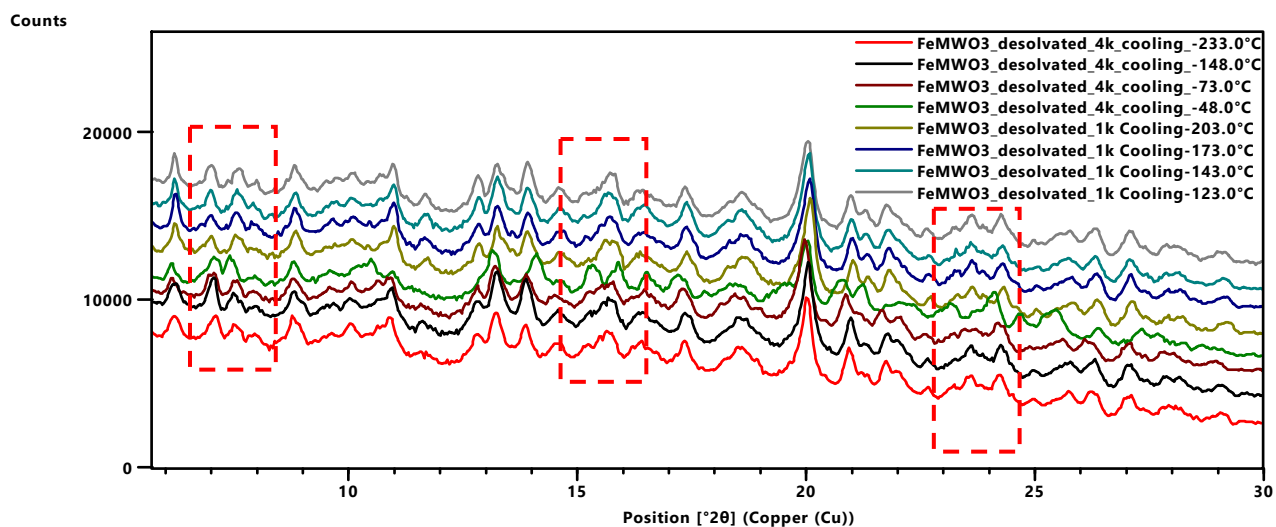


**Figure S19.** Comparison of powder patterns of desolvated **1** at 1 K min<sup>-1</sup> and 4 K min<sup>-1</sup> cooling rates. The main regions of difference is highlighted in the red boxes.

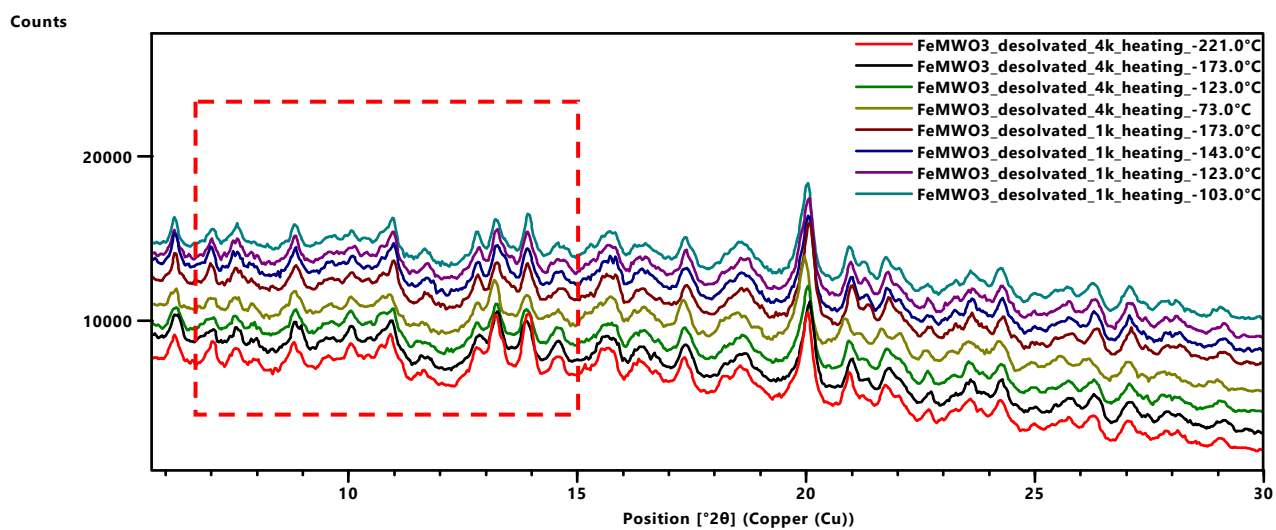


**Figure S20.** Comparison of powder patterns of desolvated **1** at 1 K min<sup>-1</sup> and 4 K min<sup>-1</sup> heating rates. The main region of difference is highlighted in the red box.

### S9.3. PXRD lattice parameters

**Table S8.** Lattice parameters of  $1 \cdot 6\text{H}_2\text{O}$  with  $1 \text{ K min}^{-1}$  scan rate. Scans are shown in the order they were performed in the variable temperature experimental run.

Temperature (K)	a (Å)	b (Å)	c (Å)	$\alpha$ (°)	$\beta$ (°)	$\gamma$ (°)	Volume (Å <sup>3</sup> )
250 (cooling)	16.3966	17.4306	21.2877	77.735	86.799	71.855	5649.2
200 (cooling)	16.3753	17.3868	21.0361	77.379	88.791	72.703	5574.1
150 (cooling)	16.0243	16.4073	20.5219	95.301	91.383	105.283	5185.7
100 (cooling)	16.0147	16.3585	20.5073	95.196	91.174	104.785	5168.3
75 (cooling)	16.0342	16.3236	20.4855	95.793	90.898	104.684	5161.2
45 (cooling)	16.0659	16.3179	20.3354	96.242	90.606	104.423	5139.3
20 (cooling)	16.0305	16.3128	20.1074	95.675	89.451	105.067	5058.9
48 (heating)	16.0131	16.3270	20.2845	96.289	89.918	105.181	5103.5
75 (heating)	16.0946	16.3275	20.5818	95.416	91.276	105.644	5195.1
100 (heating)	16.3682	16.3533	20.6192	94.485	91.978	106.473	5262.6
150 (heating)	16.2043	16.5440	20.7581	95.504	91.784	106.079	5312.9
200 (heating)	16.1763	17.4998	20.8910	80.996	90.789	73.155	5587.0
250 (heating)	16.2925	17.5300	20.9087	78.715	87.180	71.891	5584.3
298 (heating)	16.4363	17.5005	21.2366	78.575	87.327	72.178	5699.3

**Table S9.** Lattice parameters of  $1 \cdot 6\text{H}_2\text{O}$  with  $4 \text{ K min}^{-1}$  scan rate. Scans are shown in the order they were performed in the variable temperature experimental run.

Temperature (K)	a (Å)	b (Å)	c (Å)	$\alpha$ (°)	$\beta$ (°)	$\gamma$ (°)	Volume (Å <sup>3</sup> )
250 (cooling)	16.2688	17.5025	20.0688	78.582	87.348	72.173	5596.6
200 (cooling)	16.2092	17.4918	21.5542	78.513	87.340	72.035	5591.2
150 (cooling)	16.1402	16.3719	20.5400	95.594	90.178	106.153	5224.5
100 (cooling)	16.1486	16.3571	20.5847	80.309	89.619	72.449	5212.8
75 (cooling)	16.1504	16.3535	20.6237	79.897	89.514	72.318	5097.8
45 (cooling)	16.1105	16.3238	20.5459	79.888	89.354	72.301	5087.4
20 (cooling)	16.0976	16.3201	20.4999	79.760	88.486	71.994	5042.7
60 (heating)	16.3617	16.5903	20.6240	95.534	91.382	106.233	5342.3
75 (heating)	16.1553	16.3341	20.5816	95.130	91.258	105.741	5200.4
100 (heating)	16.1735	16.3952	20.5912	95.551	91.141	105.904	5226.6
150 (heating)	16.3435	16.6697	20.7569	95.890	90.797	106.318	5396.1
200 (heating)	16.5637	17.5002	21.0366	78.707	87.617	71.431	5669.3
250 (heating)	16.4099	17.5044	21.1416	78.873	87.251	72.169	5669.7
298 (heating)	16.5034	17.5998	21.1921	78.092	86.985	72.819	5768.0

**Table S10.** Lattice parameters of desolvated **1** with 1 K min<sup>-1</sup> scan rate. Scans are shown in the order they were performed in the variable temperature experimental run.

Temperature (K)	a (Å)	b (Å)	c (Å)	$\alpha$ (°)	$\beta$ (°)	$\gamma$ (°)	Volume (Å <sup>3</sup> )
298 (cooling)	16.2039	16.8025	20.4887	80.424	89.351	72.340	5236.9
285 (cooling)	16.2155	16.7946	20.4675	80.350	89.413	72.503	5236.1
255 (cooling)	16.2204	16.8078	20.4392	80.389	89.573	72.494	5234.2
220 (cooling)	16.2232	16.7937	20.4166	80.211	89.654	72.609	5225.0
190 (cooling)	16.1950	16.6959	20.4502	79.939	89.509	72.886	5198.0
170 (cooling)	16.1199	16.5549	20.4335	80.017	89.407	72.749	5123.9
150 (cooling)	16.1220	16.3927	20.3921	80.000	89.778	72.933	5067.3
130 (cooling)	16.0944	16.3651	20.3402	80.181	89.760	72.892	5039.2
100 (cooling)	16.0780	16.3497	20.3385	80.077	89.569	72.631	5020.6
70 (cooling)	16.0565	16.2652	20.3351	80.209	89.593	72.594	4988.4
100 (heating)	16.1141	16.4274	20.1953	80.171	89.586	72.776	5025.5
130 (heating)	16.1407	16.4280	20.1937	80.118	89.744	72.780	5040.5
150 (heating)	16.1814	16.5763	20.2194	79.922	89.502	72.738	5093.5
170 (heating)	16.1875	16.6051	20.4405	80.060	89.454	72.680	5161.3
190 (heating)	16.2175	16.7079	20.4727	80.125	89.541	72.541	5209.0
220 (heating)	16.2173	16.7721	20.4176	79.978	89.398	72.555	5212.2
255 (heating)	16.2300	16.7978	20.4398	80.308	89.469	72.398	5230.6
285 (heating)	16.2279	16.7838	20.4812	80.361	89.593	72.446	5238.0
300 (heating)	16.2426	16.8042	20.4603	80.408	89.618	72.484	5245.5

**Table S11.** Lattice parameters of desolvated **1** with 4 K min<sup>-1</sup> scan rate. Scans are shown in the order they were performed in the variable temperature experimental run.

Temperature (K)	a (Å)	b (Å)	c (Å)	$\alpha$ (°)	$\beta$ (°)	$\gamma$ (°)	Volume (Å <sup>3</sup> )
250	16.2434	16.8569	20.4888	80.378	89.653	72.356	5265.1
225	16.2182	16.8182	20.4502	80.203	89.800	72.474	5234.7
200	16.1588	16.6778	20.3946	79.939	89.471	72.815	5164.8
125	16.1096	16.5056	20.3028	80.018	89.704	72.706	5070.2
50	16.0962	16.5005	20.3026	80.270	89.903	72.620	5065.2
52	16.1099	16.5515	20.2337	80.173	89.637	72.450	5067.7
100	16.1666	16.5891	20.2462	80.017	89.504	72.537	5101.4
150	16.1685	16.6558	20.2460	80.052	89.636	72.605	5123.5
200	16.1513	16.7570	20.4152	80.001	89.251	72.663	5189.0
225	16.2121	16.8304	20.4068	80.380	89.873	72.618	5232.5
250	16.2172	16.8338	20.4170	80.488	89.681	72.448	5233.6
271	16.2357	16.8358	20.4316	80.526	89.639	72.291	5240.0
298	16.2558	16.8464	20.4623	80.376	89.417	72.108	5252.0

## S10. References

1. I.A. Guzei, *J. Appl. Crystallogr.* 2014, **47**, 806-809.
2. Z.G. Lada, *Magnetochemistry*. 2022, **8**, 108.
3. G.M. Sheldrick, *Acta. Cryst. C.* 2015, **71**, 3–8.
4. H. Min, A.R. Craze, T. Taira, M.J. Wallis, M.M. Bhadbhade, R. Tian, D.J. Fanna, R. Wuhrer, S. Hayami, J.K. Clegg, C.E. Marjo, L.F. Lindoy, F. Li, *Chemistry*. 2022, **4**, 535-547.
5. H. Min, A.R. Craze, M.J. Wallis, R. Tokunaga, T. Taira, Y. Hirai, M.M. Bhadbhade, D.J. Fanna, C.E. Marjo, S. Hayami, L.F. Lindoy, and F. Li, *Chem. Eur. J.* 2023, In press. <https://doi.org/10.1002/chem.202203742>.
6. M. Wallis, H. Min, L. F. Lindoy, and F. Li, *Molecules*, 2023, **28**, 1404.